

# Pulsed heterodyne Brillouin microscopy enables high-specificity, low-phototoxicity biomechanical imaging with single-ended access

Zi-Xuan Du<sup>1,2,†</sup>, Shuai Yao<sup>1,2,†</sup>, Yun Qi<sup>1,2,\*</sup>, Jin-Rui Zhang<sup>1,2</sup>, Jun-Lin You<sup>1,2</sup>, Zhisheng Yang<sup>3,\*</sup>, Ting Mi<sup>4</sup>, Jingjing Xie<sup>4</sup>, Wei-Biao Chen<sup>1,2</sup>, Long Zhang<sup>1,2</sup>, Fan Yang<sup>1,2,\*</sup>

<sup>1</sup> Shanghai Institute of Optics and Fine Mechanics, Chinese Academy of Sciences, Shanghai, China.

<sup>2</sup> University of Chinese Academy of Sciences, Beijing, China.

<sup>3</sup> State Key Laboratory of Information Photonics & Optical Communications, Beijing University of Posts and Telecommunications, Beijing, China.

<sup>4</sup> School of Physical Science and Technology & State Key Laboratory of Advanced Medical Materials and Devices, ShanghaiTech University, Shanghai, China.

<sup>†</sup> These authors contributed equally to this work

Correspondence should be addressed to Y.Q. ([qiyun@siom.ac.cn](mailto:qiyun@siom.ac.cn)), Z.Y. ([zhisheng.yang@bupt.edu.cn](mailto:zhisheng.yang@bupt.edu.cn)) or F.Y. ([yang@siom.ac.cn](mailto:yang@siom.ac.cn)).

**Brillouin microscopy (BM) enables three-dimensional, non-contact viscoelastic imaging with high spatial resolution. Since its introduction in 2008, different BM modalities have balanced accessibility and spectral performance. Spontaneous BM offers single-ended access but limited spectral resolution, while stimulated BM provides higher resolution but requires a dual-objective configuration, restricting sample types and thicknesses. Heterodyne BM combines single-ended access with high spectral resolution, yet its demand for high optical power (276 mW) and long pixel dwell time (100 ms) limits biological applications. Here, we present pulsed heterodyne Brillouin microscopy (PHBM), which reduces excitation energy by two orders of magnitude while maintaining high spectral resolution and precision. Using only 10 mW average power and 10 ms pixel dwell time, PHBM achieves 27 MHz intrinsic spectral resolution and 10 MHz shift precision in water. The low phototoxicity of PHBM enables imaging of sensitive single cells, revealing subcellular mechanical features. Moreover, we resolve double Brillouin peaks with frequency separations as small as 200 MHz, demonstrating high mechanical specificity. High-quality imaging of *ex vivo* porcine cornea further highlights the benefits of single-ended access for thick and complex tissues. The high-resolution, high-accuracy, calibration-free, alignment-free, compact and robust characteristics of PHBM opens new opportunities in biomedical research.**

Mechanical properties critically influence cellular and tissue behavior and function [1-3]. Quantifying viscoelastic parameters such as stiffness and viscosity is essential for understanding mechanisms of development, regeneration, and disease progression [4]. However, existing techniques for measuring biomechanics face key limitations. Atomic force microscopy (AFM) infers quasi-static Young's modulus from cantilever deflection [5], providing high lateral resolution but averaging the axial response and requiring model-dependent interpretation. In contrast, elastography techniques such as ultrasound, magnetic resonance imaging, and optical coherence elastography are noninvasive but limited in spatial resolution, hindering subcellular measurements [6].

Spontaneous Brillouin scattering, an inelastic light-acoustic interaction (Fig. 1a), provides a non-contact means to probe viscoelastic properties through analysis of the Brillouin spectrum. Tandem Fabry-Pérot interferometers offer high spectral resolution (~100 MHz) [7,8] but require long acquisition times (>10 s per spectrum) [9], making them impractical for bio-

imaging applications [10]. The advent of the virtual image phased array (VIPA) spectrometer in 2008 increased acquisition speed by nearly two orders of magnitude [10], establishing Brillouin microscopy as a powerful biomechanical imaging tool [11-14] with applications spanning single-cell mechanics [15-17], corneal assessment *ex vivo* [18] and *in vivo* [19, 20], plant biology [21], cancer [22], skin mechanics [23], and tissue regeneration [24]. Subsequent advances in line-scanning [25, 26] and full-field multiplexing [27] have further improved throughput, yet the limited spectral resolution ( $\sim 300$  MHz) [25-28] constrains mechanical specificity and quantitative accuracy.

Stimulated Brillouin scattering (SBS) microscopy avoids diffraction-based spectral analysis through pump–probe interactions, achieving higher spectral resolution [29-32]. Pulsed SBS further improves sensitivity and speed [33-35] but requires dual-objective geometries and is restricted to imaging depths of  $\sim 100$ – $200$   $\mu\text{m}$ , limiting biological applicability [13,35].

Heterodyne Brillouin microscopy, inspired by coherent Doppler LIDAR [36] and fibre-optic sensing [37], detects optical beating to achieve high spectral resolution with single-ended (epi) access [38]. However, previous biological implementations required high continuous-wave power ( $\sim 276$  mW) and long pixel dwell time ( $\sim 100$  ms) [38], leading to phototoxicity and long acquisition durations ( $>16$  min for  $100 \times 100$  pixels).

Here, we present pulsed heterodyne Brillouin microscopy (PHBM), which overcomes these limitations. Guided by quantitative noise analysis, we propose and demonstrate that increasing the pump peak power enables shot-noise-limited detection of spontaneous Brillouin scattering at drastically reduced optical dose-achieved here for the first time in heterodyne Brillouin microscopy. PHBM achieves 10 MHz Brillouin shift precision and 27 MHz spectral resolution using only 10 mW average power and 10 ms pixel dwell time in water. We further demonstrate high-specificity, low-phototoxicity live-cell imaging with high spatial resolution ( $0.62 \times 0.61 \times 2.41 \mu\text{m}^3$ ), as well as high-quality imaging of thick corneal tissue.

## Results

### Pulsed heterodyne Brillouin microscopy: scheme and setup

To elucidate how pulsed excitation enhances heterodyne Brillouin microscopy, we quantitatively analyzed the system noise characteristics. In conventional continuous-wave (CW) heterodyne Brillouin microscopy, the spontaneous Brillouin signal is generated by a CW pump and detected through optical beating with a CW local oscillator (LO) on a balanced photodetector (BPD). The beat signal is digitized and processed using a fast Fourier transform (FFT, see Methods for details).

Building on our recently established general noise model for heterodyne detection [39], we derived a simplified expression for the Brillouin microscopy configuration (Supplementary Note 1 and Note 2). For a fixed FFT segment and pump duration of  $T$ , the signal-to-noise ratio (SNR) can be written as:

$$SNR \propto \frac{\mathcal{R}_p^2 P_{LO} \bar{P}_{sp} \sqrt{T}}{\sqrt{\frac{\pi \gamma_B \mathcal{R}_p^2 P_{LO} \bar{P}_{sp} \sigma_e^2}{2} + \frac{\pi^2 \gamma_B^2 \sigma_e^4}{16}}} \quad (1)$$

where  $\mathcal{R}_p$  is the BPD responsivity,  $P_{LO}$  the LO power,  $\bar{P}_{sp}$  the average spontaneous Brillouin power in each segment, and  $\gamma_B$  the Brillouin linewidth. The detection noise spectral density is

$\sigma_e^2 \approx \sigma_T^2 + 2q\mathcal{R}_p P_{LO}$ , including thermal noise  $\sigma_T^2$  and LO shot noise  $2q\mathcal{R}_p P_{LO}$ , with  $q$  being the elementary charge.

To maximize the SNR,  $P_{LO}$  was set to 9 mW so that LO shot noise dominates (Supplementary Fig. 1), giving  $\sigma_e^2 \approx 2q\mathcal{R}_p P_{LO}$ . Under this condition, Eq. (1) simplifies to:

$$SNR \propto \frac{A\bar{P}_{sp}\sqrt{T}}{\sqrt{B\bar{P}_{sp}+C}} \quad (2)$$

where A, B and C are constants independent of the pump power.

When the pump power is not sufficiently high—as in previous CW heterodyne studies using  $\sim 300$  mW [38]—the second term in the denominator of Eq. (2) dominates (Supplementary Note 2), such that:

$$SNR \propto \bar{P}_{sp}\sqrt{T} \propto P_{Pump}\sqrt{T} \propto \sqrt{P_{Pump}E} \quad (3)$$

where  $E = P_{Pump}T$  is the pump optical energy. This relation highlights a key energy-efficiency principle: for a fixed SNR, increasing the pump power linearly reduces the required optical energy. For example (Fig. 1b, upper panel), increasing the pump power from 0.1 W to 1 W allows the acquisition time accelerating from 10 ms (yellow curve) to 100  $\mu$ s (blue curve), improving the energy efficiency by a factor of 10.

Although higher pump power reduces the energy required per pixel and could, in principle, enable high-speed imaging with rapid scanning, a CW beam with high instantaneous intensity can induce local photodamage during the brief dwell time within the sample. To mitigate this, we distribute the same peak power into a pulse train with reduced average power, maintaining the same SNR due to the linear dependence of spontaneous heterodyne Brillouin scattering. For example, a 100- $\mu$ s effective exposure can be implemented as a 10-ms pulse train with 1 W peak power and 10 mW average power (1/100 duty cycle; Fig. 1b, lower panel). Considering the trade-off between spectral broadening and achievable peak power (Supplementary Fig. 2), we employed pulse durations of 20–40 ns.

When the pump peak power exceeds  $\sim 20$  W, the first term in the denominator of Eq. (2) dominates (Supplementary Note 1), resulting in:

$$SNR \propto \sqrt{\bar{P}_{sp}T} \propto \sqrt{P_{Pump}T} \propto \sqrt{E} \quad (4)$$

This relation indicates a truly shot-noise-limited spontaneous Brillouin detection regime—analogous to that achieved in confocal VIPA Brillouin microscopy. Notably, previous CW heterodyne studies that reported “shot-noise-limited” performance [38] referred only to LO shot-noise dominance, rather than Brillouin-signal shot-noise limitation, which is realized here for the first time (Supplementary Fig. 3).

It is widely assumed in spontaneous Brillouin microscopy that pulsed excitation cannot improve energy efficiency because spontaneous Brillouin scattering is a linear effect. Contrary to this belief, we show that pulses with elevated pump peak power substantially enhance energy efficiency—simultaneously reducing optical power and accelerating acquisition—while enabling Brillouin-signal shot-noise-limited performance.

We emphasize that the pulse enhancement observed in PHBM arises solely from reaching this Brillouin-signal shot-noise limited regime. This mechanism fundamentally differs from the pulse enhancement in stimulated Brillouin microscopy, where the improvement arises from the nonlinear gain of stimulated Brillouin scattering [33–35].

A schematic of the experimental setup is shown in Fig. 1c, with full details provided in Supplementary Fig. 4. The pulsed pump beam (Fig. 1d) is focused into the sample through a high-numerical-aperture (0.7) objective, producing a focal volume of  $0.62 \times 0.61 \times 2.41 \mu\text{m}^3$  (see spatial-resolution characterization in Supplementary Fig. 5 and Methods). The backscattered Brillouin light interferes with the LO beam and is detected by a balanced photodetector. The frequency offset is carefully selected such that the intermediate frequency lies within the bandwidth of both the photodetector and digitizer (Fig. 1e and Methods). The heterodyne signal is directly digitized and processed for spectral retrieval (Methods and Supplementary Fig. 6).

### Validation of the pulse-enhancement scheme

To experimentally validate the pulse-enhancement mechanism, we measured Brillouin spectra of water with a fixed total acquisition time of 10 ms and a 36 ns pulse width, while varying peak pump power from 3.5 W to 28 W (corresponding to duty cycles of  $2.3\% \rightarrow 0.036\%$  and average powers of  $80 \text{ mW} \rightarrow 10 \text{ mW}$ ; Fig. 1f). The Brillouin shift precision remained  $\sim 8 \text{ MHz}$  up to  $\sim 14 \text{ W}$  peak power, confirming that this regime is dominated by detection noise (term  $C$  in Eq. (2)). In this range, increasing the peak power enables proportional reduction of the average power without loss of precision (Supplementary Note 2).

At peak powers above  $\sim 14 \text{ W}$ , the precision begins to degrade when the average power is proportionally reduced, indicating a transition into the Brillouin-signal shot-noise-limited regime. These observations are in excellent agreement with theoretical predictions (Supplementary Note 2 and Supplementary Fig. 7). Under the optimized condition of 28 W peak power, 36 ns pulse width, 0.036% duty cycle (10 mW average power), PHBM achieves 10 MHz Brillouin shift precision, 27 MHz spectral resolution and 10 ms full-spectrum acquisition time for water (a representative spectrum in Fig. 1g). Importantly, the optical power and acquisition-time performance of PHBM are comparable to state-of-the-art confocal VIPA-based Brillouin microscopes [15,20,21], while offering substantially higher spectral resolution.

For direct comparison, we also measured the Brillouin shift precision as a function of pump power using a VIPA-based confocal Brillouin microscope with a setup similar to that of Ref. [40]. The measured slope of -0.47 (Supplementary Fig. 8) agrees closely with the predicted  $\sqrt{E}$  scaling in Eq. (4), confirming the shot-noise limited performance of the VIPA system. These results further verify that PHBM achieves true Brillouin-signal shot-noise-limited detection at significantly lower average optical power and shorter pixel dwell time than previous reported CW heterodyne implementations [38].

### Laser system for PHBM

To realize the pulse-enhancement scheme, we developed a dual-wavelength laser system consisting of a pulsed pump laser and a CW LO (Fig. 2 and Methods). In PHBM, spectral broadening originates from two sources: (1) the finite fast Fourier transform (FFT) window applied to the temporal signal, which is the dominate contribution, and (2) the Fourier broadening of the optical pulse itself (Methods and Supplementary Fig. 2a, b). This behavior contrasts with pulsed stimulated Brillouin scattering (SBS) microscopy, where pulse-induced

Fourier broadening is the primary limitation on spectral resolution [35]. For instance, using 6 ns pulses-typical in pulsed SBS systems-would induce 165 MHz of spectral broadening (Supplementary Fig. 2a, b). To maintain high spectral resolution, we therefore employed longer pulses of 20-40 ns.

Compared with the configuration in Ref. [35], three key technical advances were implemented (Methods): (1) extended pulse duration (20-40 ns) to suppress Fourier broadening and improve spectral resolution. (2) Acousto-optic modulator (AOM)-based pulse generation to eliminate transient distortions introduced by semiconductor optical amplifier (SOA). (3) 976 nm pump for optical amplification, which enhances erbium absorption and shortened the gain fibre, thereby increasing the SBS threshold of the fibre and maximizing the achievable peak power. Together, these improvements yield a 70% increase in the peak power compared with the previous system [35].

Note that both the pump and LO originate from telecom-band (1560 nm) seed lasers and fibre amplifiers, allowing the use of cost-effective components and efficient frequency doubling via standard periodically poled lithium niobate (Methods).

### Characterization of PHBM

To evaluate the spectral resolution of PHBM, we first measured the heterodyne beating between the pulsed pump and the CW LO (Supplementary Fig. 2a-c). The full width at half maximum of the beating spectrum was 27 MHz for a 36 ns pulse width (Supplementary Fig. 2a, b), confirming a spectral resolution of 27 MHz, as both seed lasers have linewidths below 100 kHz.

We further verified the frequency accuracy of the spectrometer by comparing the beating frequency between two single-frequency CW lasers measured using a frequency counter with that retrieved from PHBM. The two values agreed within 0.1 MHz, demonstrating the excellent frequency accuracy of our detection scheme.

To validate the spectral fidelity, we performed side-by-side measurements with varying numerical apertures (NAs) using both PHBM and a stimulated Brillouin scattering (SBS) microscope configured following Ref. [33]. The Brillouin linewidths measured under both low- and high- NA objectives showed excellent agreement between the two systems (Supplementary Fig. 9 and Supplementary Fig. 10). Notably, unlike SBS microscopy, PHBM is not affected by lock-in amplifier-induced broadening, a common broadening factor in SBS systems [14,33].

### Comparison between PHBM and confocal VIPA Brillouin microscopy

To benchmark spectral specificity in imaging, we compared PHBM with a VIPA-based confocal Brillouin microscope by measuring the Brillouin spectra at the interface between NaCl solution and agarose (Fig. 3a-g). PHBM clearly resolved two distinct peaks at 5.11 GHz (5% agarose) and 5.77 GHz (10.7% NaCl water solution) (Fig. 3b) at the interface, whereas the VIPA system produced a single broadened peak at the same position (Fig. 3e). This comparison highlights the substantially higher spectral resolution of PHBM, which enables discrimination between mechanically distinct materials within the focal volume.

We also evaluated long-term stability under free-running conditions over 110 minutes. In the confocal VIPA system, the Brillouin shift of water drifted by ~40 MHz under laboratory conditions (Fig. 3h), owing to the strong temperature dependence of VIPA dispersion. As a result, additional optical path with standard materials [12] or electro-optic modulators [41] are commonly required for continuous calibration. In contrast, our PHBM exhibited only a ~2 MHz

drift over the same period under free running (Fig. 3h), attributable to minor pump-LO frequency drift and slight temperature variations of the water sample. This result demonstrates the exceptional intrinsic stability of PHBM without the need for active stabilization.

### **PHBM imaging of living cells with high specificity and low phototoxicity**

To demonstrate the applicability of PHBM to biomechanical imaging, we performed measurements on live NIH/3T3 fibroblasts (Fig. 4) and HeLa cells (Supplementary Fig. 11). For fibroblasts, brightfield, Brillouin shift, linewidth, and peak amplitude images (Fig. 4a-d) were acquired using an average optical power of 30 mW and a pixel dwell time of 10 ms. Under these conditions, PHBM clearly resolved subcellular mechanical features, including distinct contrasts between the cytoplasm, nucleus, and nucleoli. Both lateral (Fig. 4f) and axial (Fig. 4g) Brillouin shift profiles revealed substantial spatial heterogeneity.

Operating in the shot-noise-limited regime (Eq. (4)), PHBM maintains equivalent SNR-and thus comparable Brillouin shift precision and image quality-under different exposure-power tradeoffs. Under the same peak-power condition, a higher-average power/shorter-exposure setting (30 mW, 10 ms) yielded equivalent performance to a lower-average power/longer-exposure setting (10 mW, 30 ms), as further confirmed in Supplementary Fig. 12.

We observed double-peaked Brillouin spectra at interfaces between mechanically distinct regions. At the cell-medium boundary, a representative spectrum (Fig. 4h) exhibited peaks at 5.05 GHz (medium) and 5.25 GHz (cell). A similar dual-peak feature was observed at the nucleolus–nucleoplasm boundary (Fig. 4i). These results underscore the high spectral resolution and specificity of PHBM in capturing subtle mechanical heterogeneity within living cells.

We next assessed phototoxicity using propidium iodide (PI), a standard viability marker (Fig. 4j-n) [28]. PHBM generated high-quality Brillouin maps with clear subcellular contrast (Fig. 4k), and no detectable PI fluorescence was observed 50 minutes after imaging (n=20), confirming the cell membrane integrity and low phototoxicity of the PHBM. In contrast, dead-cell controls exhibited strong PI fluorescence (Fig. 4m, n), validating the assay.

### **PHBM imaging of porcine cornea *ex vivo***

To demonstrate the single-ended accessibility of PHBM, we imaged porcine cornea *ex vivo* using an effective NA of 0.24 (Fig. 5). A  $300 \times 300 \mu\text{m}^2$  region near the cornea-medium interface was scanned (Fig. 5a). The Brillouin shift map (Fig. 5b) revealed higher shifts in the epithelium compared to the stroma, consistent with previous report [42]. The Brillouin shift precision within the adjacent medium was 6.9 MHz (white-outlined region in Fig. 5b), underscoring the high detection sensitivity of PHBM.

Representative spectra acquired at the cornea-medium boundary exhibited well-resolved double peaks (Fig. 5c), corresponding to Brillouin shifts of 5.15 GHz (L1, PBS medium) and 5.58 GHz (L2, epithelium). Spectra obtained within the medium and the stroma are shown in Fig. 5d and Fig. 5e, respectively. These results demonstrate the high spectral resolution and sensitivity of PHBM and highlight its potential for quantitative assessment of corneal biomechanics relevant to clinical applications. Further studies are required to evaluate phototoxicity associated with pulsed pump illumination, particularly in clinical contexts.

## Discussions

In summary, we have demonstrated that increasing the pump peak power in PHBM enables a substantial reduction in the optical dose delivered to the sample while maintaining identical SNR. Compared with conventional CW heterodyne Brillouin microscopy [38], PHBM achieves an order-of-magnitude lower average optical power and a tenfold increase in pixel acquisition speed, without compromising spectral or spatial resolution. We validated the high spectral resolving power and low phototoxicity through live-cell imaging, and further demonstrated single-ended accessibility in corneal tissue.

A quantitative comparison with previously reported spontaneous Brillouin modalities is provided in Supplementary Table 1. Notably, compared with confocal VIPA Brillouin microscopy—which is widely adopted in both scientific and commercial settings—PHBM offers three key advantages.

- (1) Higher spectral resolution without requiring additional power or dwell time compared to state-of-the-art confocal VIPA systems [15,20,21], enabling enhanced mechanical specificity and improved discrimination of subcellular viscoelastic features within heterogeneous focal volumes.
- (2) Absolute frequency referencing via heterodyne detection and Fourier-domain analysis, eliminating the need for external calibration elements such as water standards [12] or electro-optic modulators [41].
- (3) Compact and robust system architecture, built entirely from polarization-maintaining fibre, including both the laser source and spectrometer. This design provides excellent alignment stability, minimal maintenance and markedly reduced temperature sensitivity, as no temperature-dependent etalon transmission occurs.

While PHBM does not match the acquisition speed of pulsed SBS or full-field Brillouin modalities, its intrinsic epi-detection capability provides key advantages for imaging optically thick or structurally complex specimens. This single-ended configuration allows straightforward integration with standard inverted or upright fluorescence microscopes and broadens compatibility with common biological sample formats.

Two current limitations remain relative to confocal VIPA systems (Supplementary Note 4). First, the spectral measurement bandwidth is narrower: the present 1.25 GHz detection range is constrained by the digitizer sampling speed. Increasing this to 2.5 GHz would broaden the accessible range to 4.5–7 GHz at 780 nm, full covering the Brillouin spectral span of most biological specimen. Second, PHBM requires an external pulsed pump laser. Nevertheless, the compact laser module—including the 1560 nm pulsed pump, 780 nm CW LO, and all associated drivers—fits within a  $62 \times 48 \times 46$  cm<sup>3</sup> enclosure (Supplementary Fig. 13), preserving overall system practicality.

Future developments could further enhance PHBM performance. For example, incorporating a carrier-suppressed electro-optic modulator for double-sideband LO generation could double detected signal amplitude by simultaneously capturing Stokes and anti-Stokes components (Supplementary Note 4). Comprehensive studies of cellular responses—including stress signaling, proliferation, and genomic stability—will also be important to ensure that pulsed excitation does not introduce subtle biological phototoxicity. In addition, integrating the

standalone pulsed SHG module directly into the laser-source enclosure will further compact the system, improving portability and enabling true plug-and-play operation.

Overall, PHBM combines high spectral precision, low phototoxicity, single-ended accessibility, and operational robustness. Its compact design and compatibility with established optical microscopy platforms position PHBM as a versatile and scalable modality for biomechanical imaging in living systems.

## ACKNOWLEDGMENTS

F.Y. acknowledges the Young Scientists Fund from National Natural Science Foundation of China (NSFC). F.Y., L.Z. and Y.Q. acknowledge the supports from Strategic Priority Research Program of the Chinese Academy of Sciences (XDB0650000) and Shanghai Institute of Optics and Fine Mechanics. We acknowledge Dr. J. Li from Shanghai Ninth People's Hospital, Shanghai Jiao Tong University School of Medicine, Department of Ophthalmology for technical assistance in processing the porcine cornea samples *ex vivo*. We also thank the staff of a local slaughterhouse for providing porcine corneas used in this study.

## AUTHOR CONTRIBUTIONS

F.Y. initialized and conceived the project. Z.-X.D. built the heterodyne Brillouin microscope with help from J.-L.Y. F.Y., Z.-X.D. and Y.Q. developed the pulse-enhancement theory of heterodyne microscopy with help from Z.Y. S.Y. built the VIPA-based Brillouin microscope for side-by-side comparison. Y.Q. built the laser source system. J.-R.Z. and Z.-X.D. wrote the code. Z.-X.D. performed experiments and analyzed data. T.M. and J.X. provided cell samples and helped with the interpretation. F.Y., L.Z. and W.-B.C. led the project. F.Y., Z.-X.D. and Y.Q. wrote the paper with input from all authors.

## COMPETING INTERESTS

F.Y., Z.-X.D. and Y.Q. are inventors of patents related to the technology described in this paper. All other authors declare no competing interests.

## REFERENCES

1. Chaudhuri, O., Cooper-White, J., Janmey, P.A. *et al.* Effects of extracellular matrix viscoelasticity on cellular behaviour. *Nature* **584**, 535–546 (2020).
2. Fan, W., Adebowale, K., Váncza, L. *et al.* Matrix viscoelasticity promotes liver cancer progression in the pre-cirrhotic liver. *Nature* **626**, 635–642 (2024).
3. Barriga, E., Franze, K., Charras, G. *et al.* Tissue stiffening coordinates morphogenesis by triggering collective cell migration *in vivo*. *Nature* **554**, 523–527 (2018).
4. Nia, H.T., Munn, L.L. & Jain, R.K. Probing the physical hallmarks of cancer. *Nat. Methods* **22**, 1800–1818 (2025).
5. Franz, C.M., Puech, PH. Atomic Force Microscopy: A Versatile Tool for Studying Cell Morphology, Adhesion and Mechanics. *Cel. Mol. Bioeng.* **1**, 289–300 (2008).
6. Kennedy, B. F., Wijesinghe, P. & Sampson, D. D. The emergence of optical elastography in biomedicine. *Nat. Photonics* **11**, 215–221 (2017).
7. Lindsay, S. M., Anderson, M. W. & Sandercock, J. R. Construction and alignment of a high performance multipass vernier tandem Fabry–Perot interferometer. *Rev. Sci. Instrum.* **52**, 1478–1486 (1981).
8. Mattana, S. *et al.* Non-contact mechanical and chemical analysis of single living cells by microspectroscopic techniques. *Light Sci. Appl.* **7**, 17139–17139 (2018).
9. Scarponi, F. *et al.* High-performance versatile setup for simultaneous Brillouin–Raman microspectroscopy. *Phys. Rev. X* **7**, 031015 (2017).

10. Scarcelli, G., Yun, S. Confocal Brillouin microscopy for three-dimensional mechanical imaging. *Nature Photon.* **2**, 39–43 (2008).
11. Prevedel, R., Diz-Muñoz, A., Ruocco, G. *et al.* Brillouin microscopy: an emerging tool for mechanobiology. *Nat. Methods.* **16**, 969–977 (2019).
12. Zhang, J., Scarcelli, G. Mapping mechanical properties of biological materials via an add-on Brillouin module to confocal microscopes. *Nat. Protoc.* **16**, 1251–1275 (2021).
13. Kabakova, I., Zhang, J., Xiang, Y. *et al.* Brillouin microscopy. *Nat. Rev. Methods Primers* **4**, 8 (2024).
14. Bouvet, P., Bevilacqua, C., Ambekar, Y. *et al.* Consensus statement on Brillouin light scattering microscopy of biological materials. *Nat. Photon.* **19**, 681–691 (2025).
15. Scarcelli, G., Polacheck, W., Nia, H. *et al.* Noncontact three-dimensional mapping of intracellular hydromechanical properties by Brillouin microscopy. *Nat. Methods.* **12**, 1132–1134 (2015).
16. Elsayad, K. *et al.* Mapping the subcellular mechanical properties of live cells in tissues with fluorescence emission-Brillouin imaging. *Sci. Signal.* **9**, rs5 (2016).
17. Antonacci, G. *et al.* Background-deflection Brillouin microscopy reveals altered biomechanics of intracellular stress granules by ALS protein FUS. *Commun. Biol.* **1**, 139 (2018).
18. Scarcelli, G. *et al.* Brillouin microscopy of collagen crosslinking: noncontact depth-dependent analysis of corneal elastic modulus. *Invest. Ophthalmol. Vis. Sci.* **54**, 1418–1425 (2013).
19. Scarcelli, G. & Yun, S. H. In vivo Brillouin optical microscopy of the human eye. *Opt. Express* **20**, 9197 (2012).
20. Zhang, H. *et al.* Motion-tracking Brillouin microscopy for in-vivo corneal biomechanics mapping. *Biomed. Opt. Express* **13**, 6196–6210 (2022).
21. Keshmiri, H., Cikes, D., Samalova, M. *et al.* Brillouin light scattering anisotropy microscopy for imaging the viscoelastic anisotropy in living cells. *Nat. Photon.* **18**, 276–285 (2024).
22. Margueritat, J. *et al.* High-frequency mechanical properties of tumors measured by Brillouin light scattering. *Phys. Rev. Lett.* **122**, 018101 (2019).
23. Romodina, M. N., Parmar, A. & Singh, K. In vivo measurement of the biomechanical properties of human skin with motion-corrected Brillouin microscopy. *Biomed Opt Express* **15**, 1777–1784 (2024).
24. Schlüßler, R. *et al.* Mechanical mapping of spinal cord growth and repair in living zebrafish larvae by brillouin imaging. *Biophys. J.* **115**, 911–923 (2018).
25. Bevilacqua, C. *et al.* High-resolution line-scan Brillouin microscopy for live imaging of mechanical properties during embryo development. *Nat. Methods* **20**, 755–760 (2023).
26. Zhang, J. *et al.* Rapid biomechanical imaging at low irradiation level via dual line-scanning Brillouin microscopy. *Nat. Methods* **20**, 677–681 (2023).
27. Bevilacqua, C., Prevedel, R. Full-field Brillouin microscopy based on an imaging Fourier-transform spectrometer. *Nat. Photon.* **19**, 494–501 (2025).
28. Antonacci, G. *et al.* Recent progress and current opinions in Brillouin microscopy for life science applications. *Biophys. Rev.* **12**, 615–624 (2020).
29. Remer, I. *et al.* High-sensitivity and high-specificity biomechanical imaging by stimulated Brillouin scattering microscopy. *Nat. Methods* **17**, 913–916 (2020).
30. Shaashoua, R., Kasuker, L., Kishner, M. *et al.* Brillouin gain microscopy. *Nat. Photon.* **18**, 836–841 (2024).
31. Rosvold, J. R. *et al.* Stimulated Brillouin scattering flow cytometry. *Biomed. Opt. Express* **15**, 6024–6035 (2024).

32. Shaashoua, R. et al. Enhancing mechanical stimulated Brillouin scattering imaging with physics-driven model selection. *Laser Photonics Rev.* **18**, 2301054 (2024).
33. Yang, F. et al. Pulsed stimulated Brillouin microscopy enables high-sensitivity mechanical imaging of live and fragile biological specimens. *Nat. Methods* **20**, 1971–1979 (2023).
34. Chow, D. M. & Yun, S.-H. Pulsed stimulated Brillouin microscopy. *Opt. Express* **31**, 19818–19827 (2023).
35. Qi, Y. et al. Stimulated Brillouin scattering microscopy with a high-peak-power 780-nm pulsed laser system. *Nat. Photon.* **19**, 879–887 (2025).
36. Menzies, R. T., Hardesty, R. M. Coherent Doppler lidar for measurement of wind fields. *Proc. IEEE* **77**, 449–462 (1989).
37. Shimizu, K. et al. Coherent self-heterodyne detection of spontaneously Brillouin-scattered light waves in a single-mode fiber. *Opt. Lett.* **18**, 185–187 (1993).
38. Taylor, M. A. et al. Heterodyne Brillouin microscopy for biomechanical imaging. *Biomed. Opt. Exp.* **12**, 6259–6268 (2021).
39. Jin, S. et al. A Framework for Spontaneous Brillouin Noise: Unveiling Fundamental Limits in Brillouin Metrology. Preprint at <https://doi.org/10.48550/arXiv.2505.17651> (2025).
40. Bo, Y., et al. Angle dependence of Brillouin scattering intensity in liquids. *Opt. Lett.* **50**, 2502–2505 (2025).
41. Testi, C. et al. Electro-optic modulator source as sample-free calibrator and frequency stabilizer for Brillouin microscopy. Preprint at <https://arxiv.org/abs/2412.20516> (2024).
42. Scarcelli, G., Pineda, R. & Yun, S. H. Brillouin optical microscopy for corneal biomechanics. *Invest. Ophthalmol. Vis. Sci.* **53**, 185–190 (2012).

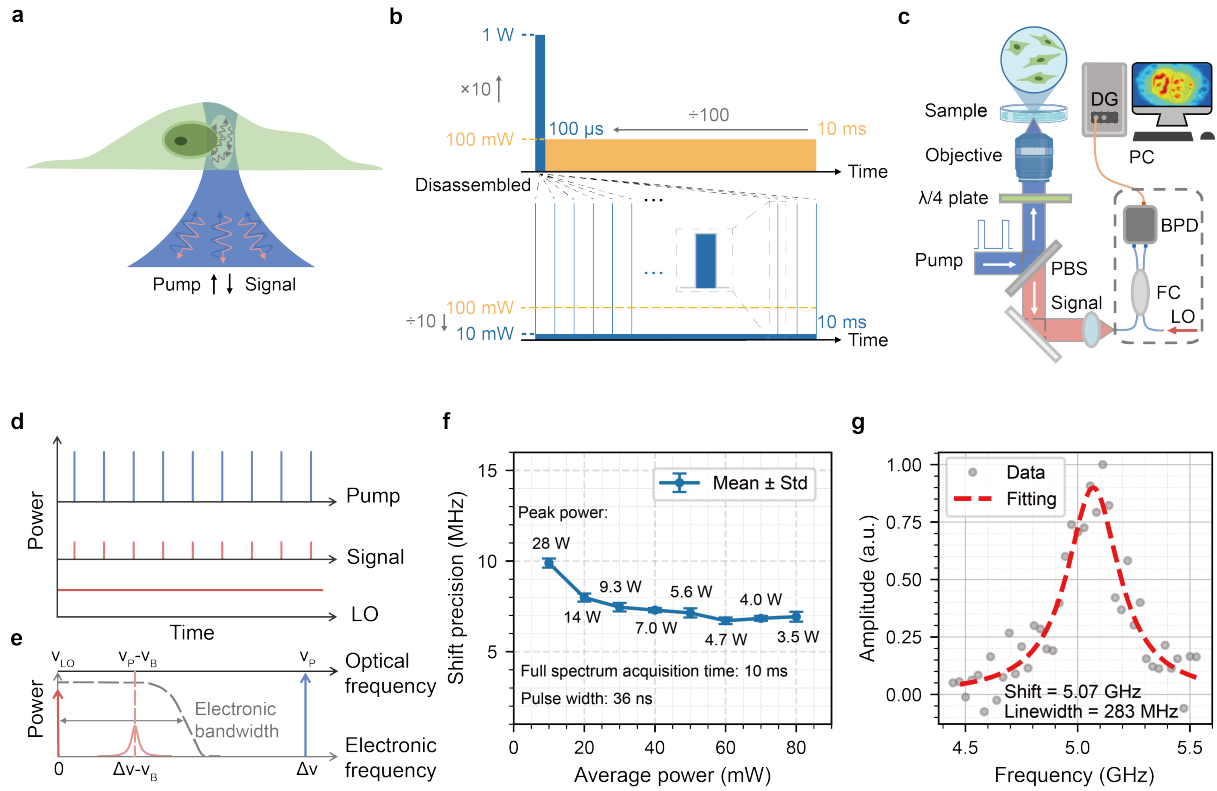


**Fig. 1 Pulsed heterodyne Brillouin microscopy (PHBM) approach and performance.** **a**, Backward spontaneous Brillouin scattering within sample induced by a focused laser beam. **b**, Schematic illustration of the optical power and exposure time required for heterodyne detection with same SNR. Increasing the power tenfold (from 100 mW to 1 W) while reducing the acquisition time by a factor of 100 (i.e., an overall tenfold decrease in excitation energy) yields the same SNR performance, when the constant noise term (the second term in the denominator of Eq. (2)) dominates. Disassembling the 100- $\mu$ s continuous laser into a sequence of uniformly distributed pulses within 10 ms reduces the average power to 10 mW (blue area in the lower panel), which is one-tenth of the orange CW pump laser. **c**, Schematic of PHBM setup. PBS: polarizing beam splitter; LO: local oscillator; FC: 50:50 polarization-maintaining fibre coupler; BPD: balanced photodetector; DG: digitizer; PC: personal computer. The pulsed pump is focused into the sample to generate a spontaneous Brillouin scattering signal, whose backward-propagating components are reflected by the PBS and coupled into the fibre. The signal fibre is connected to the heterodyne spectrometer. The beating signal generated by the signal and LO is detected by a BPD, and the electronic signal is sampled by the digitizer which is integrated in a computer case. **d**, Time-domain distribution of pulsed pump, pulsed signal and CW LO. **e**, Frequency-domain distribution of pulsed pump, pulsed signal and CW LO. The frequency difference between the local oscillator and the Brillouin signal lies within the electronic bandwidth of the detection system. **f**, Measured Brillouin shift precision of water as a function of average power and peak power for the heterodyne spectrometer. Error bars represent the standard deviation of five independent measurements, each statistically estimated from  $n = 400$  spectra. The full spectrum acquisition time and pulse width were fixed at 10 ms and 36 ns, respectively. **g**, Typical spectrum of water obtained from PHBM under 10 mW average power, 10 ms exposure time, 28 W peak power and 36 ns pulse width using a low-NA (0.12) objective.

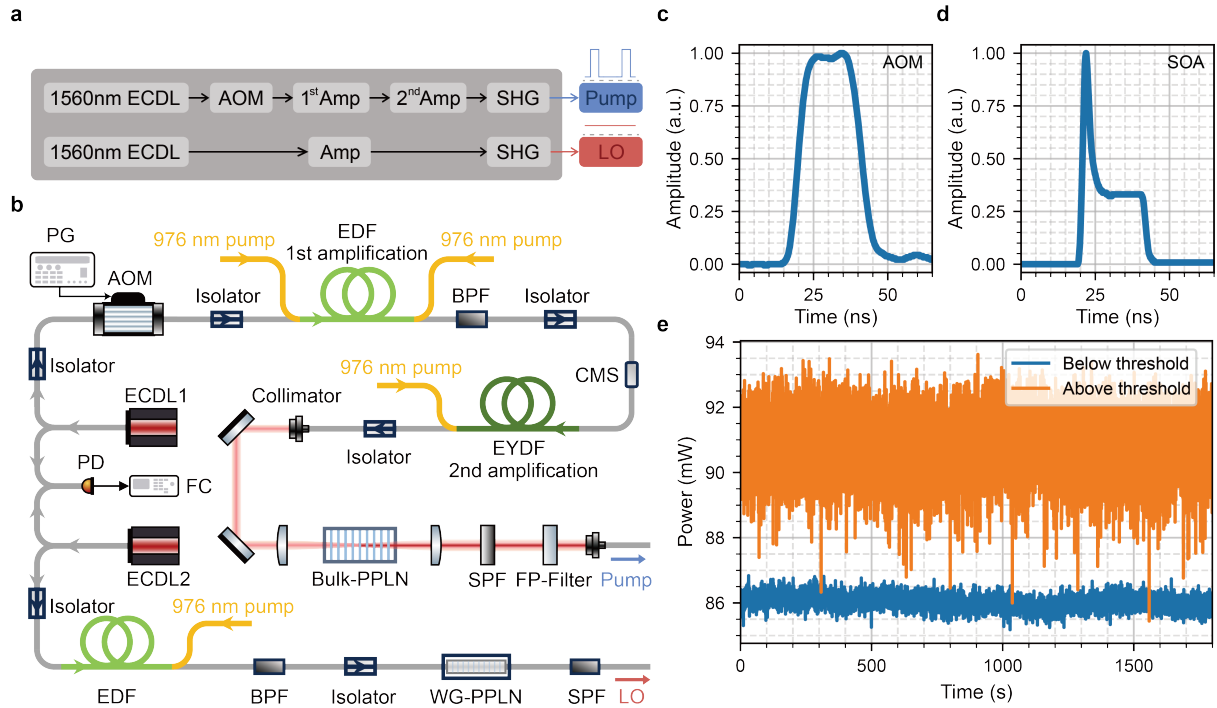


**Fig. 2 Setup and performance of the laser system for PHBM.** **a**, Schematic of the laser system for PHBM including a pulsed pump beam and a continuous wave local oscillator (LO). ECDL: external cavity diode laser; AOM: acousto-optic modulator; Amp: light amplification; SHG: second-harmonic generation. **b**, Detailed experimental setup of the laser system for PHBM. ECDL1 and ECDL 2 are used as seed lasers for pump and LO respectively. Light from ECDL1 is chopped by an AOM to generate several tens of nanosecond pulse in this work. The pulsed beam is amplified by two stage light amplification, with 1<sup>st</sup> amplification by an EDF (Erbium-doped fibre) and 2<sup>nd</sup> amplification by an EYDF (Erbium/Ytterbium doped fibre). Then the 780 nm pump beam is generated by SHG with a bulk-PPLN (periodically poled lithium niobate). The ECDL2 1560 nm seed laser is first amplified by an EDF and then SHG with a WG (waveguide)-PPLN. A FC (frequency counter) is used to monitor the frequency difference between the two 1560 nm seed lasers. PD: photodetector; BPF: bandpass filter; WG-PPLN: waveguide-periodically poled lithium niobate; SPF: short-pass filter; CMS: cladding mode stripper. **c,d**, Temporal profiles of a 25.6 ns amplified pulse seeded by AOM chopping (**c**) and semiconductor optical amplifier (SOA) (**d**). **e**, Average power stability of the constructed pulsed laser over 30 minutes. The stimulated Brillouin scattering (SBS) effect of the fibre limits the output peak power; when the peak power exceeds the SBS threshold (yellow curve), the intensity noise increases dramatically.

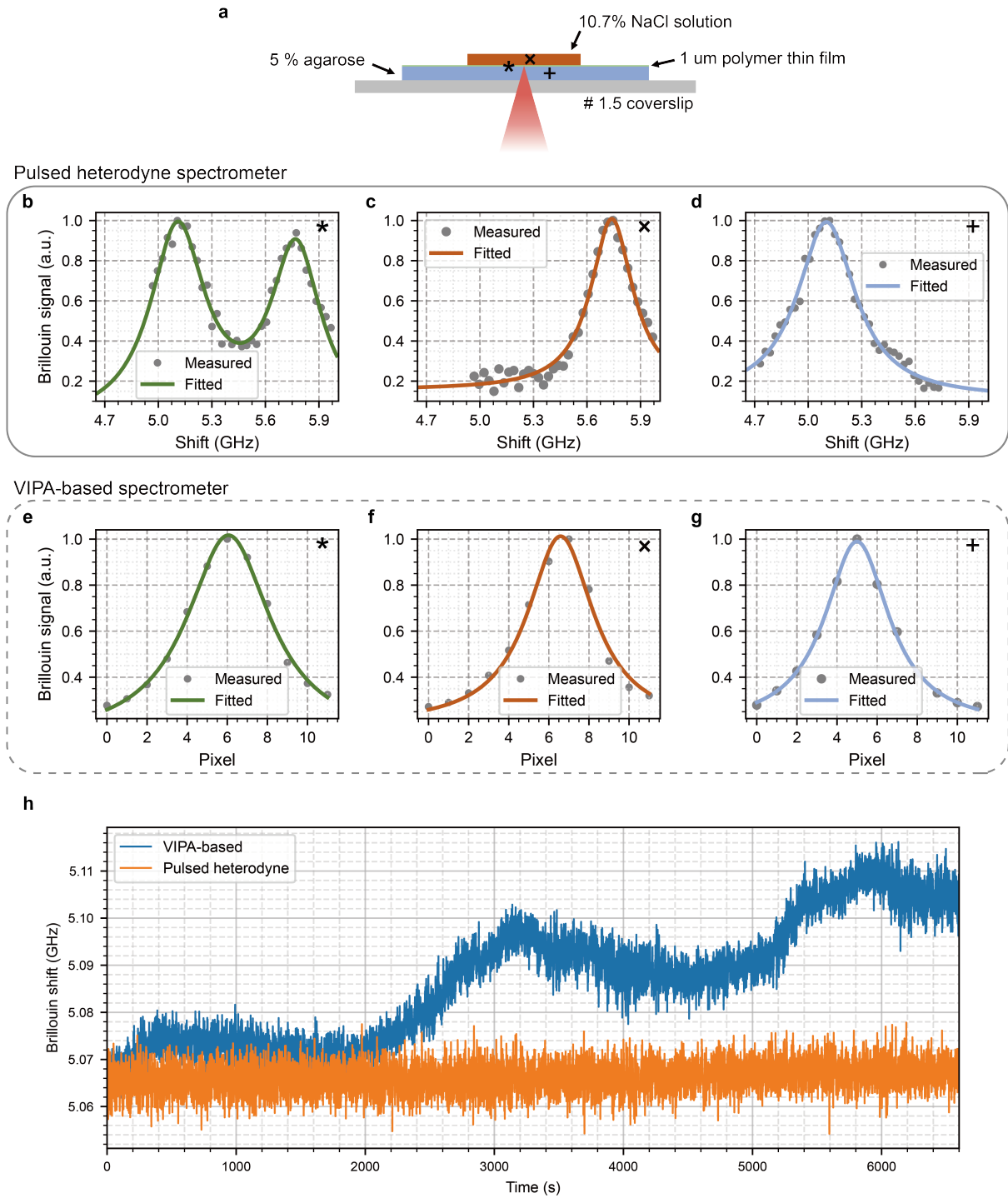


**Fig. 3 Side-by-side comparison of our PHBM with VIPA-based confocal Brillouin microscope. a**, Schematic diagram of the NaCl solution and agarose interface. The polymer thin film prevents the penetration of NaCl solution into agarose. **b**, A representative spectrum retrieved by PHBM at the interface between 10.7% NaCl solution and 5% agarose, marked by an asterisk in **a**. **c**, A representative spectrum of NaCl solution retrieved by PHBM, marked by a cross in **a**. **d**, A representative spectrum of agarose retrieved by PHBM, marked by a plus sign in **a**. Note that the frequency of LO was slightly shifted for better visualization of agarose Brillouin spectrum. **e**, A representative Brillouin spectrum retrieved by the VIPA-based spectrometer at the interface between 10.7% NaCl solution and 5% agarose, marked by an asterisk in **a**. **f**, A representative Brillouin spectrum of NaCl solution retrieved by VIPA-based

spectrometer, marked by a cross in **a**. **g**, A representative Brillouin spectrum of agarose retrieved by VIPA-based spectrometer, marked by a plus sign in **a**. All measurements (**b-g**) were performed with the same average power (60 mW), exposure time (50 ms) and a low-NA (0.24) objective. For PHBM (**b-d**), the peak power and pulse width were set to 28 W and 36 ns, respectively. **h**, Long term performance comparison of the water Brillouin shift with our PHBM and confocal VIPA Brillouin microscope over 110-minutes. The experiments were conducted in a temperature-controlled laboratory (25 °C, approximately stable within a few degrees) and with a same low-NA (0.12) objective. We performed a single calibration at the beginning of the experiment. The calibration of the VIPA-based spectrometer was performed by using the positions of the elastic scattering peak and the Brillouin peak of a reference sample (water in this experiment) on the camera to establish a mapping between camera pixels and frequency. For the PHBM, calibration was achieved by recording the beating frequency between the LO and pump lasers with a frequency counter and using this value to recover the spectral coordinates of the measured spectra (see Methods for details). To ensure high shift precision, the average power and pixel time were set to 10 mW and 100 ms, respectively, with a peak power of 28 W, a pulse width of 36 ns, and a repetition rate of 10 kHz for the PHBM. For the VIPA-based spectrometer measurement, a 35-mW pump power and 100 ms pixel time were used. The slight increase (~2 MHz) observed in the curve of pulse heterodyne scheme is attributed to the frequency drift between the pump and LO lasers as well as the slight temperature change of the water.

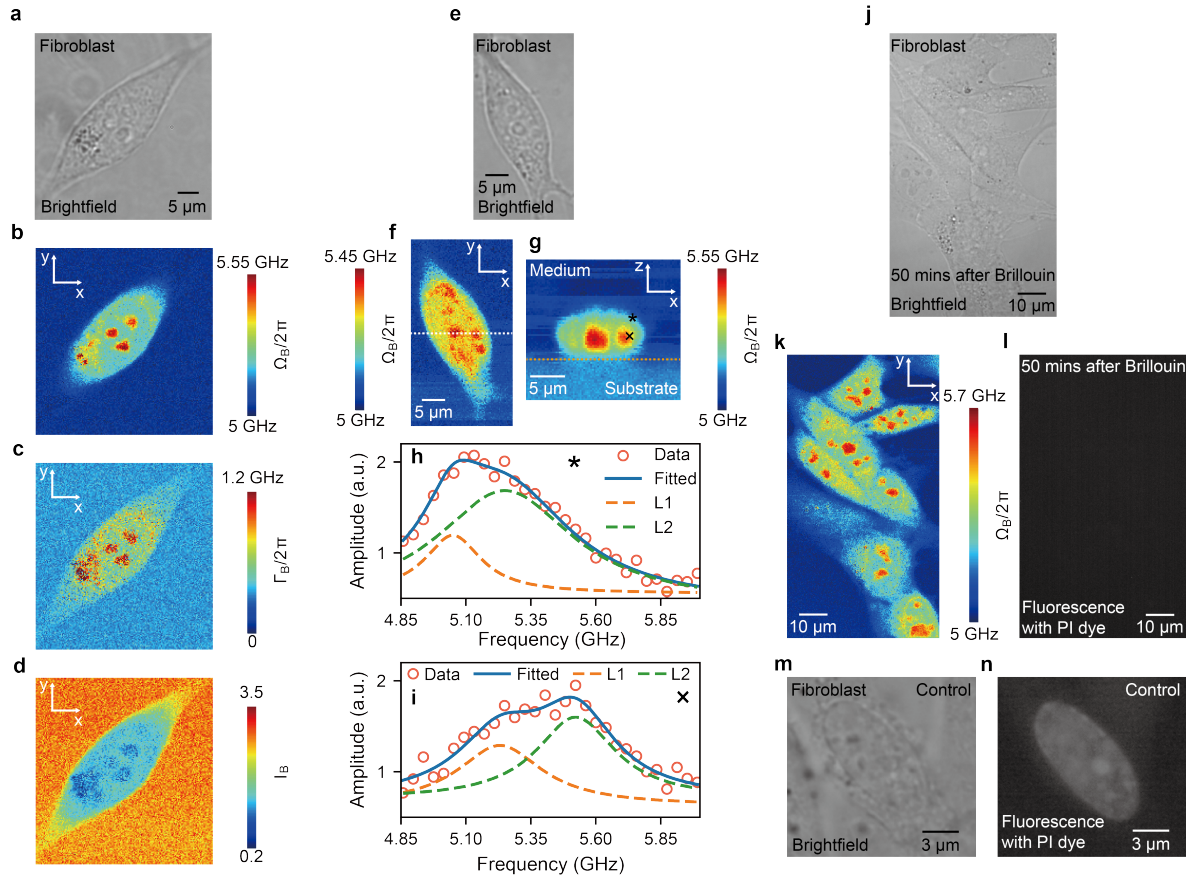


**Fig. 4 PHBM imaging of cultured fibroblast cells.** **a-d**, Brightfield (**a**), Brillouin shift (**b**), linewidth (**c**) and intensity (**d**) of the imaged fibroblast cell attached to glass. The average power on sample and exposure time are respectively 30 mW and 10 ms, with scan range of  $42 \mu\text{m} \times 44 \mu\text{m}$  and scan step of  $0.25 \mu\text{m} \times 0.25 \mu\text{m}$ . **e**, Brightfield of a fibroblast cell attached to PAA-based gel. **f**, Brillouin shift image of the fibroblast cell in x-y plane with imaging condition of 30 mW average power and 10 ms pixel time. **g**, Brillouin shift image of the fibroblast cell in x-z plane along the white dashed line shown in **f**. The orange dashed line indicates the interface of cultured medium and substrate. An average power of 30 mW and a pixel time of 60 ms were used to improve the SNR and enable recognition of the double peak from noise. **h**, A representative Brillouin spectrum at the boundary of medium and cytoplasm marked by an asterisk in **g**. The raw data and its double-Lorentzian fitting are shown as red circles and a solid blue curve, respectively. The two constituting components (L1 and L2) are plotted as dashed lines. **i**, A representative Brillouin spectrum at the boundary of nucleoplasm and nucleolus marked by a cross in **g**. The raw data and its double-Lorentzian fitting are shown as red circles and a solid blue curve, respectively. The two constituent components (L1 and L2) are plotted as dashed lines. Offsets are added to L1 and L2 in both **h** and **i** for better visualization. **j, k**, Brightfield (**j**) and Brillouin shift (**k**) images of a fibroblast cell cluster attached to glass. **l**, The fluorescence image of the fibroblast cell cluster 50 minutes after Brillouin imaging. Absence of fluorescence from PI dye indicates the viability of the imaged cell cluster. **m, n**, The brightfield (**m**) and corresponding fluorescence (**n**) images of a fibroblast cell in the control group. The effectiveness of the PI dye was confirmed by detecting a pronounced fluorescence signal from a dead cell.

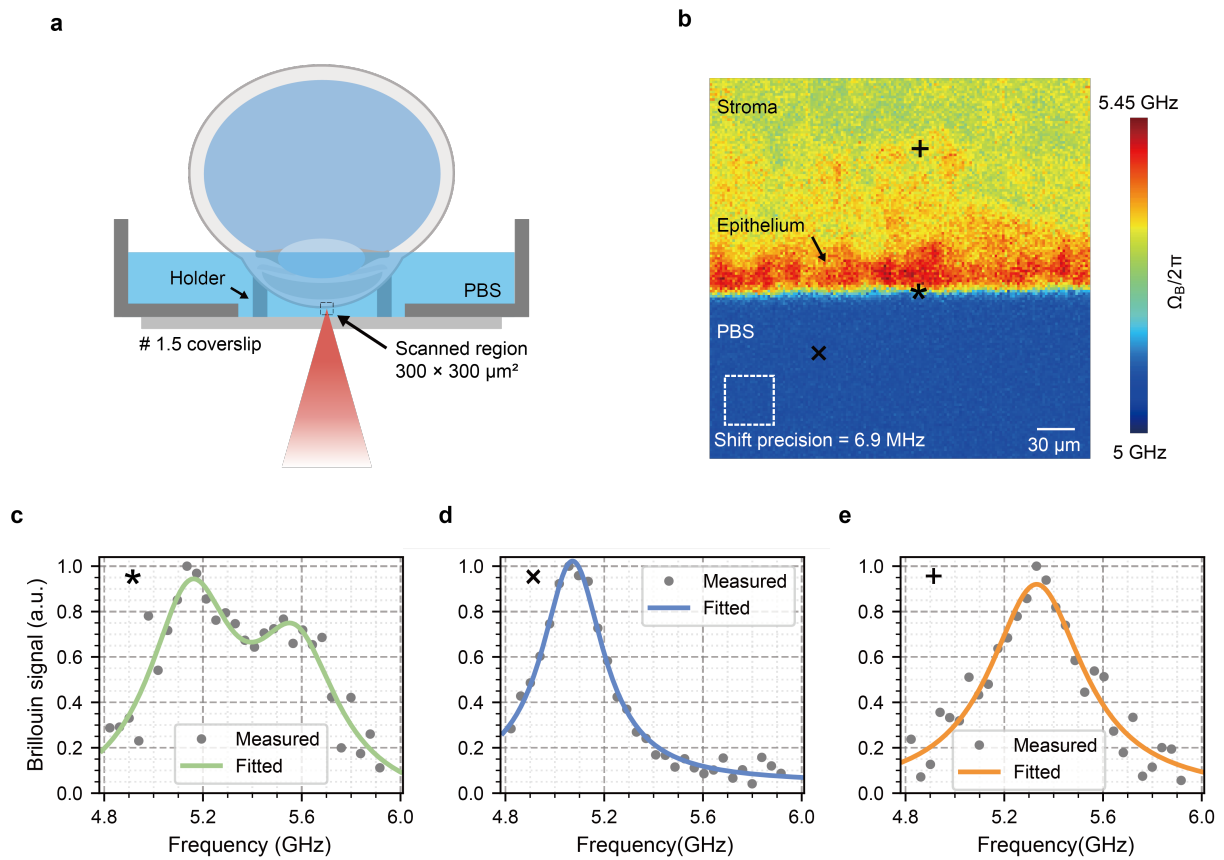


**Fig. 5 PHBM imaging of porcine cornea *ex vivo*.** **a**, Illustration of a porcine eye inversely immersed in PBS buffer using a circular silicone holder, with the imaging region indicated by a black dashed box. Note that due to the limited travel range of the piezo stage, only a  $300 \times 300 \mu\text{m}^2$  area near the cornea–medium interface was scanned rather than the entire corneal region. **b**, Brillouin shift image of the scanned region. The average power and pixel dwell time were 10 mW and 30 ms, respectively, with a scan step of  $2 \mu\text{m} \times 2 \mu\text{m}$ . **c**, Representative normalized Brillouin spectrum at the interface between the corneal epithelium and PBS medium, fitted with a double Lorentzian line shape (marked by an asterisk in **b**). **d**, Representative normalized Brillouin spectrum of the PBS medium, fitted with a single Lorentzian line shape (marked by a cross in **b**). **e**, Representative normalized Brillouin spectrum of the stroma, fitted with a single Lorentzian line shape (marked by a plus sign in **b**).

## Methods

### Laser source system

Both the pulsed pump beam and the CW LO beam are based on master oscillator power amplifier (MOPA) with subsequent second harmonic generation (SHG). The short-wave infrared (SWIR) pump seed is from an external cavity diode laser (ECDL) centering at 1560.49 nm with linewidth less than 100 kHz. It is chopped into seed pulses by an acousto-optic modulator (AOM; Fibre-Q T-M300, G&H) driven by an electronic pulse generator (DG535, Stanford Research Systems) with pulse width of tens to hundreds of nanoseconds and repetition rate of tens of kHz. The seed pulse train is pre-amplified by a piece of 2.4 m-long erbium-doped fibre (EDF; PM-ESF-7/125, Coherent) bidirectional pumped at 976 nm and then boost-amplified by a piece of Er/Yb co-doped double-cladding fibre (EYDF; PM-EYDF-10/125-XPH, Coherent) backward pumped at 976 nm with a length of 0.7 m. For the typical pulse width of 25.6 ns and repetition rate of 20 kHz, the peak power of SWIR pump pulse reaches 280 W at a pumping power of 4.4 W. The gain from first and second stage are 38 and 11 dB respectively. Compared with the previous 3.5 m-long gain fibre pumped at 940 nm in the second stage [35], the substantially shortened fibre length, together with the stronger absorption at 976 nm, leads to a 70% improvement in the peak power, which is limited by stimulated Brillouin scattering. The SWIR pulsed pump is collimated out to a beam diameter of 2 mm and then focused into a bulk crystal-periodically poled lithium niobate (BC-PPLN; MSHG1550-1.0-40, Coversion) with a plano-convex lens pair (#67-549, Edmund). The frequency-doubled pulsed pump first passes a dichroic mirror (DMSP1180, Thorlabs) to remove the residual fundamental beam. The peak SHG efficiency is measured to be 70%. Then an etalon (OP-7423-6743-2, LightMachinery) with transmittance of 80% and full-width-half-maximum (FWHM) bandwidth of  $\sim$ 450 MHz is used to suppress the frequency-doubled amplified spontaneous emission (ASE). A piece of PM780-HP fibre with length of 10 cm is then used to improve the beam quality entering the Brillouin microscope. It is worth mentioning that the semiconductor optical amplifier (SOA), which was used to generate nanosecond optical pulse [35], may not be suitable here. Due to the exciton density variation, the SOA tends to exhibit an intrinsic optical overshoot at the leading edge of the relatively long seed pulses [43, 44]. The distortion is aggravated in the following two-stage fibre amplification, where the leading edge always experiences highest gain, and becomes even severer in the SHG. The spike at the leading edge as shown in Fig. 2d broadens the linewidth and is detrimental to the spectral resolution.

The SWIR seed of LO is from another ECDL, whose frequency is down-shifted from the ECDL for pulsed pump as measured by a frequency counter (53230A, Keysight). After been amplified by a piece of EDF backward pumped at 976 nm, the LO seed is frequency doubled in a waveguide PPLN (WG-PPLN; Honclabs) with output power of 45 mW at a conversion efficiency of 12%. The CW LO is then short-pass filtered by a 780/1560 nm wavelength division multiplexer and sent to the coupler to mix with the Brillouin scattering signal for heterodyne detection. A photograph of the complete laser system, placed on a movable table, is shown in Supplementary Fig. 13b.

### PHBM and heterodyne-based spectrometer

A comprehensive schematic of the constructed PHBM is presented in Supplementary Fig. 4, with a photograph of optical setup presented in Supplementary Fig. 13c. The pulsed laser is delivered to the microscope through a 10 cm PM780-HP fibre and collimated by a fibre collimator (AFC1550-2.1-APC, LBTEK) to produce an output beam with diameter of 2.2 mm. The laser polarization is controlled to p-polarization using a sequence of a quarter-wave plate, a half-wave plate, and a polarizing beam splitter (PBS). Subsequently, another quarter-wave plate converts the beam into left-circular polarization. An achromatic Galilean beam expander

(OSAE02-T3, JCOPTIX) then enlarges the beam to 4.4 mm in diameter, fully filling the back aperture of the objective (LUCPLFLN60X, Olympus) to maximize its numerical aperture. The spontaneous Brillouin backscattered light is collected by the same objective, passes back through the beam reducer and the quarter-wave plate, and is converted into s-polarization. The reflected light from the PBS is coupled into the signal fibre via an identical fibre collimator. A photograph of the heterodyne-based spectrometer is shown in Supplementary Fig. 13d. The signal fibre and LO fibre are connected to a  $2 \times 2$ , 50:50 polarization maintaining (PM) fibre coupler whose two output ports are connected to a balanced photodetector. The output electronic signal is sampled by a 2.5 GS/s digitizer directly integrated within the computer tower, resulting in an extremely compact spectrometer with a volume of  $23 \times 15 \times 2.5$  cm<sup>3</sup>. A one-Yuan coin is placed near the fibre coupler for scale and intuitive comparison.

### Data processing and spectral calibration

To reduce data volume, the digitizer is precisely synchronized with the pump laser by receiving triggers from the same pulse generator used for the AOM in the laser source system. Consequently, the time-domain signal is sampled only when the Brillouin signal is present, i.e., within the pump laser pulse duration. To convert the time-domain signal into the Brillouin spectrum, the FFT is applied to each data segment with a fixed length determined by the pulse width (Supplementary Note 2). Because the power spectral density in heterodyne detection corresponds to the target Brillouin spectrum, the modulus of the obtained spectrum is squared to yield the Brillouin spectrum with a detection-system-dependent baseline. This baseline universally arises from the heterodyne detection system, with the contribution dominated by shot noise from the LO in the proposed PHBM case (Supplementary Fig. 1). To remove this baseline and enable more accurate fitting, once the LO power is fixed, a high-SNR background spectrum is obtained by averaging the spectra acquired over a long (typically 1 s) temporal interval without the Brillouin signal. Each measured spectrum is then background-subtracted before fitting or noise analysis. Because the background SNR is much higher than that of the measured signal, this subtraction does not noticeably degrade the overall SNR. According to the exposure time and repetition rate, the corresponding number of processed spectra are then averaged to obtain each final spectrum. The beating frequency ( $f_{LP}$ ) between the LO and the pump seed lasers (prior to chopping by the AOM) is continuously monitored by a frequency counter throughout the experiment. Note that the frequency shift introduced by the AOM (300 MHz in our laser system) should be subtracted from the frequency counter readout to obtain the actual beating frequency between LO and the pump after chopping ( $f'_{LP}$ ). In the proposed PHBM, the Stokes Brillouin peak is detected, with the LO frequency lower than that of the Brillouin signal; therefore, the frequency axis  $x_f$  should be converted as  $x'_f = 2 * f'_{LP} - x_f$  to recover the true spectral coordinates. Compared with the VIPA-based spectrometer system, this calibration procedure is considerably simpler and more accurate.

### Performance characterization of PHBM

#### Measurement of spectral resolution

The spectral resolution is evaluated by measuring the spectrum of a narrow-linewidth laser (Supplementary Fig. 2 a, b and c). The objective is replaced with a high-reflectivity mirror, while all other components remained unchanged. The pump frequency is detuned from the Rb cell absorption band, allowing the laser beam to enter the spectrometer directly without absorption. Meanwhile, the local oscillator frequency is adjusted to maintain a fixed beating frequency of 420 MHz with the pump laser. The pulse width is modulated by the pulse generator to 25.6 ns, 51.2 ns, 102.4 ns, and 204.8 ns. When varying the FFT window duration, the pulse width is fixed at 204.8 ns (Supplementary Fig. 2a), whereas when varying the pulse width, the FFT window length is kept constant; For example, the data from a 51.2 ns pulse (128

points in total) are divided into two 64-point segments for FFT processing (Supplementary Fig. 2b). It is worth noting that in PHBM, the main contribution to spectral broadening, excluding the NA-induced effect, arises from the data processing of FFT. When the sampling points are sparse and the measured laser spectrum is very narrow, zero-padding is uniformly applied before and after the acquired data to extend the total length to 512 points, allowing more accurate spectral fitting (Supplementary Fig. 2c).

Additionally, we measured the linewidth of water under different pulse widths using a low-NA (0.12) objective to further verify the spectral resolution (Supplementary Fig. 2d). After subtracting a 263.7 MHz offset, the measured trend fits well with an inverse proportional function, indicating a total spectral broadening of 35.0 MHz at a pulse width of 25.6 ns, which agrees closely with the directly measured laser linewidth of 37.7 MHz (Supplementary Fig. 2a).

### **Comparison of our PHBM and stimulated Brillouin microscopy**

To further confirm the accuracy of the Brillouin spectra obtained with our PHBM, comparison experiments for same water sample at the same room temperature were performed using PHBM and a SBS microscopy system configured like the study [33] (Supplementary Fig. 9). To minimize the pulse broadening, we used a pulse width of 60 ns in SBS microscopy for comparison, which introduces approximately 2 MHz of additional spectral broadening (Supplementary Fig. 2b). Furthermore, to eliminate the linewidth broadening induced by the lock-in amplifier, we adopted an extremely slow frequency scanning rate (150 ms for 0.15 NA and 100 ms for 0.7 NA) together with a high noise-equivalent power bandwidth of 800 Hz. For PHBM, a pulse width of 36 ns was consistently used for all measurements, resulting in a total spectral broadening of 27 MHz, comprising 4 MHz from the pulsed laser linewidth and 23 MHz from FFT processing (Supplementary Fig. 2a, b). After subtracting these contributions, the remaining linewidths of water reflect only the broadening induced by the NA.

### **Measurement of spatial resolution**

The lateral resolution is evaluated by imaging the central plane of a polymethyl methacrylate (PMMA) bead embedded in 1% (w/v) agarose. Since the Brillouin shift of PMMA is 10.8 GHz (estimated from a refractive index of 1.49 and an acoustic velocity of 2820 m/s), which is much higher than that of agarose (5.02 GHz); therefore, only the Brillouin signal from agarose is detected without spectral crosstalk. By fitting the measured spectrum, the signal amplitude distribution is obtained (Supplementary Fig. 5b). The signal amplitudes of the agarose gel across the bead boundary are further fitted with an error function along both the x and y axes, with the FWHM of the derivative of the fitted curve yielding a lateral spatial resolution of 0.62  $\mu\text{m} \times 0.61 \mu\text{m}$  (Supplementary Fig. 5c, d). The axial resolution is evaluated by imaging the interface between double-distilled water and a coverslip. Only the signal from water is detected, as the Brillouin shift of borosilicate glass ( $>20$  GHz) lies far outside the detection bandwidth. Strong reflection at the water–coverslip interface generates a large unbalanced DC component, causing saturation in the low-frequency region. To prevent this saturation from affecting the fitting accuracy, the LO frequency is shifted downward so that the water signal appears in the high-frequency region, and the low-frequency portion of the spectrum is excluded from fitting. By fitting the signal amplitude along the z direction with an error function, the axial resolution is determined to be 2.41  $\mu\text{m}$  (Supplementary Fig. 5g).

### **Determination of spectral precision**

A widely used reference sample of double-distilled water is employed to evaluate the spectral precision of the PHBM. The Brillouin signal from the water is continuously measured over n

= 400 acquisitions, and the spectral precision is determined from the standard deviation of the Lorentzian fitting centers.

Shift precision at different average and peak powers, under the same exposure time, is measured using 36-ns pulses and a low-NA objective (ACHN10XP, effective NA = 0.12). The beating frequency between the pump laser and the LO is set to 5.58 GHz, corresponding to a detected spectral range of 4.33-5.58 GHz (Fig. 1f, g). The product of average power and peak power was kept constant by adjusting the pulse repetition rate proportionally to the square of the average power.

### Sample preparation and viability test

**Chemical samples.** The water sample is prepared by drop 2 ml double-distilled water in a glass-bottomed petri dish (MatTek, P35G-1.5-14-C). The NaCl solution-agarose sample is made by first dropping 30  $\mu$ L 5% agarose on the surface of a #1.5 coverslip, before the gelling of agarose, a 1 cm  $\times$  1 cm size polymer thin film with 1  $\mu$ m thickness is attached to the agarose, followed by immediately addition of 30  $\mu$ L 10.7% w/w NaCl solution on the top flat area. To prepare the PMMA beads in agarose, the PMMA bead is first diluted to 0.1% w/v. Then 8  $\mu$ L 5% agarose is drop on the middle of a #1.5 coverslip, on which a 120- $\mu$ m-thick spacer (Grace Bio-Labs SecureSeal) is attached beforehand. 5  $\mu$ L PMMA is immediately added into the agarose drop, then another coverslip is attached by the imaging spacer for sealing the sample.

**Cells.** Cell lines were obtained from Cobioer and maintained according to the guidelines provided by the American Type Culture Collection. mouse fibroblasts (NIH/3T3, CBP60317) and Human cervical carcinoma cells (HeLa, CBP60232) were cultured in Dulbecco's modified Eagle's medium (DMEM; Gibco, 11960044) supplemented with 10% (v/v) fetal bovine serum (Gibco, A5669701) and 100 U ml<sup>-1</sup> penicillin-streptomycin (Gibco, 15070063). Cells were seeded onto glass-bottom dishes (Titan confocal petri dish, BDD012035) or polyacrylamide-gel-coated dishes (Matrigen, SV3510-EC-12) at a density of 5,000 cells cm<sup>-2</sup> and allowed to adhere overnight before imaging.

**Porcine cornea.** Porcine corneas were obtained from a local slaughterhouse and were by-products of the food industry. No live animals were used in this study. According to institutional and national guidelines, the use of animal by-products for research does not require additional ethical approval. The samples were processed ex vivo by trained personnel at the Shanghai Ninth People's Hospital, Shanghai Jiao Tong University School of Medicine, Department of Ophthalmology, and all procedures complied with relevant biosafety and ethical regulations. First, 2.5 mL of PBS was added to a petri dish, and a homemade silicone ring (8 mm inner diameter, 14 mm outer diameter, 3 mm height) was positioned at the center. A fresh porcine cornea was then carefully selected, and any remaining tissue attached to it was removed. Subsequently, the cornea was gently inverted and positioned at the center of the silicone ring, ensuring that the epithelial side was in contact with the PBS to prevent strong reflection or scattering.

**Cell viability test.** To assess cell viability under PHBM, propidium iodide (PI; Sigma-Aldrich, P4170-10MG) is added to the fibroblast culture dishes at a volume ratio of 30  $\mu$ L PI solution per 2 mL of medium. Several regions of interest (ROIs) are selected and marked using brightfield modality of PHBM system for subsequent imaging. Wide-field fluorescence images are first acquired using a dual-objective setup [35], where excitation (MF525-39, Thorlabs) and emission (MF620-52, Thorlabs) filters were placed after the light-emitting diode and before the camera, respectively, to confirm cell viability prior to Brillouin imaging. The dishes are

then transferred to the PHBM system for Brillouin imaging of all cells within the ROIs. After PHBM imaging, the dishes are returned to the fluorescence microscope to verify cell viability again.

#### **Code availability**

The spectral analysis code related with this work will be made publicly available at the point of publication.

#### **Data availability**

The raw datasets generated and/or analyzed during the current study will be made publicly available at the point of publication.

## **METHODS ONLY REFERENCES**

43. Parsonson, C. W., et al. Optimal control of soas with artificial intelligence for sub-nanosecond optical switching. *Journal of Lightwave Technology* **38**, 5563-5573 (2020).
44. Dominguez-Lopez, A., et al. Novel scanning method for distortion-free BOTDA measurements. *Opt. Exp.* **24**, 10188-10204 (2016).

# Supplementary Information for

## Pulsed heterodyne Brillouin microscopy enables high-specificity, low-phototoxicity biomechanical imaging with single-ended access

Zi-Xuan Du *et al.*

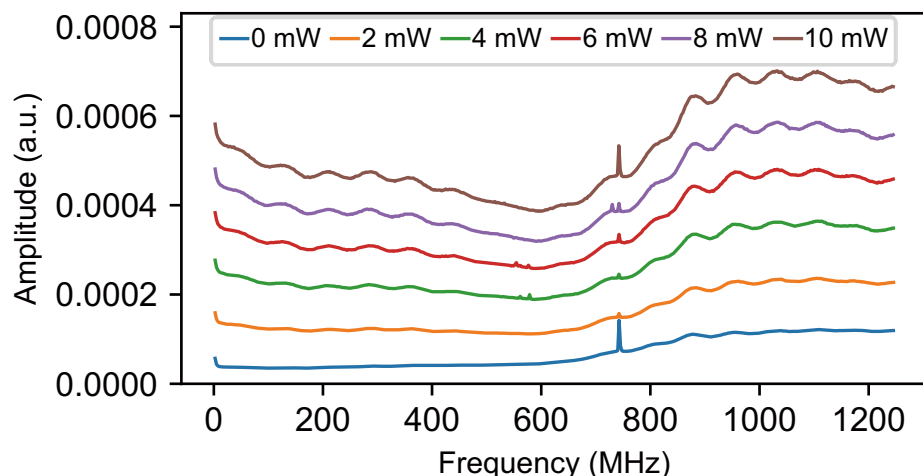
**Below Supplementary Information file includes:**

Figs. S1 to S13

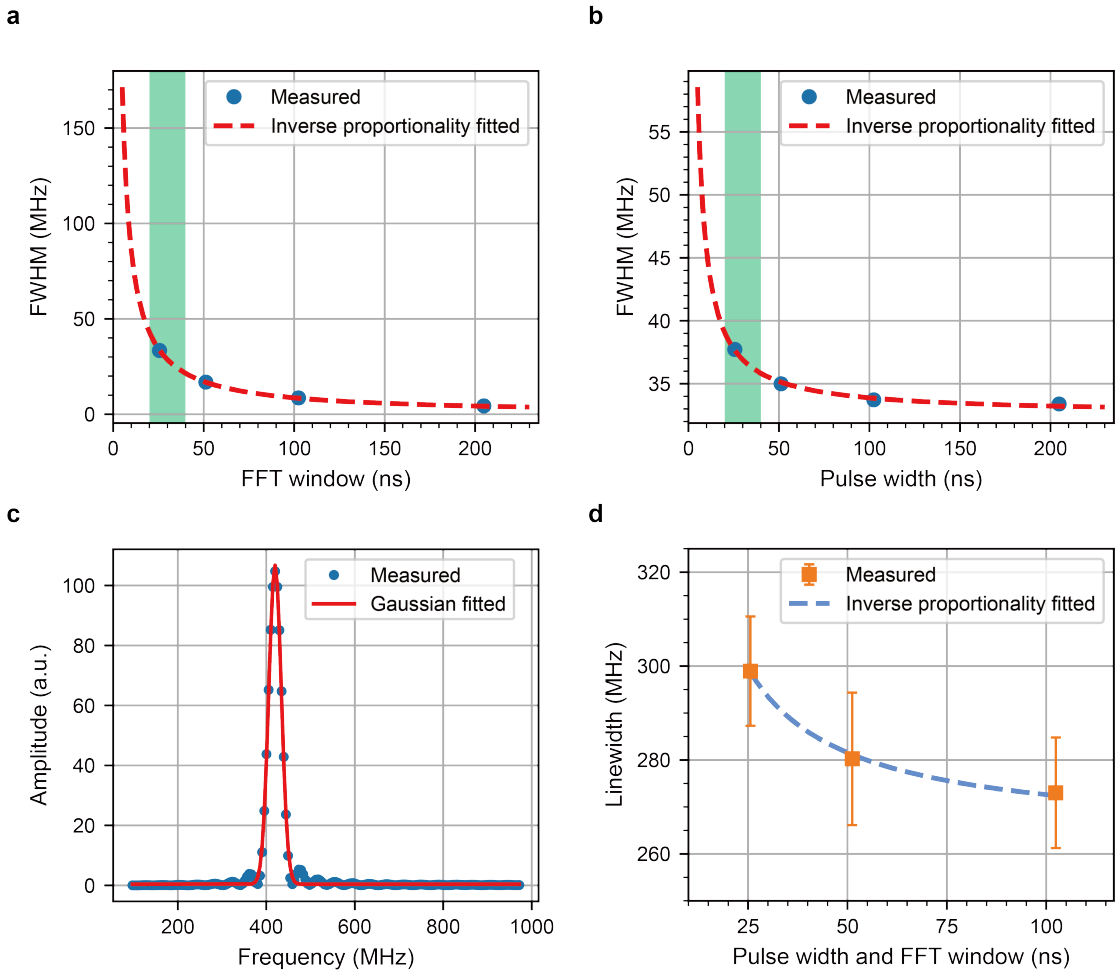
Tables S1

Notes S1 to S4

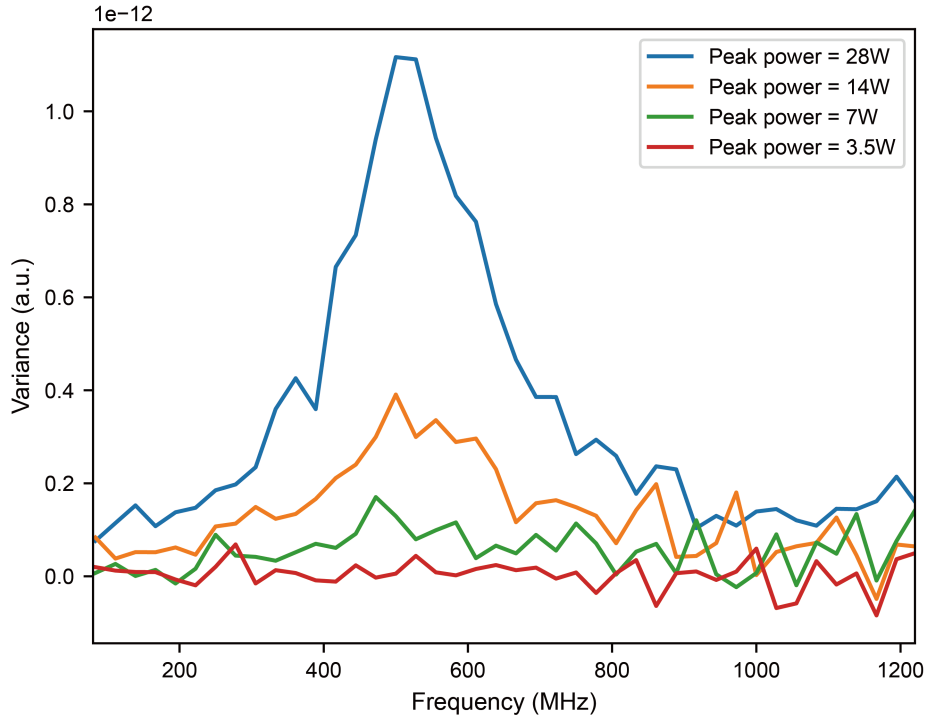
References



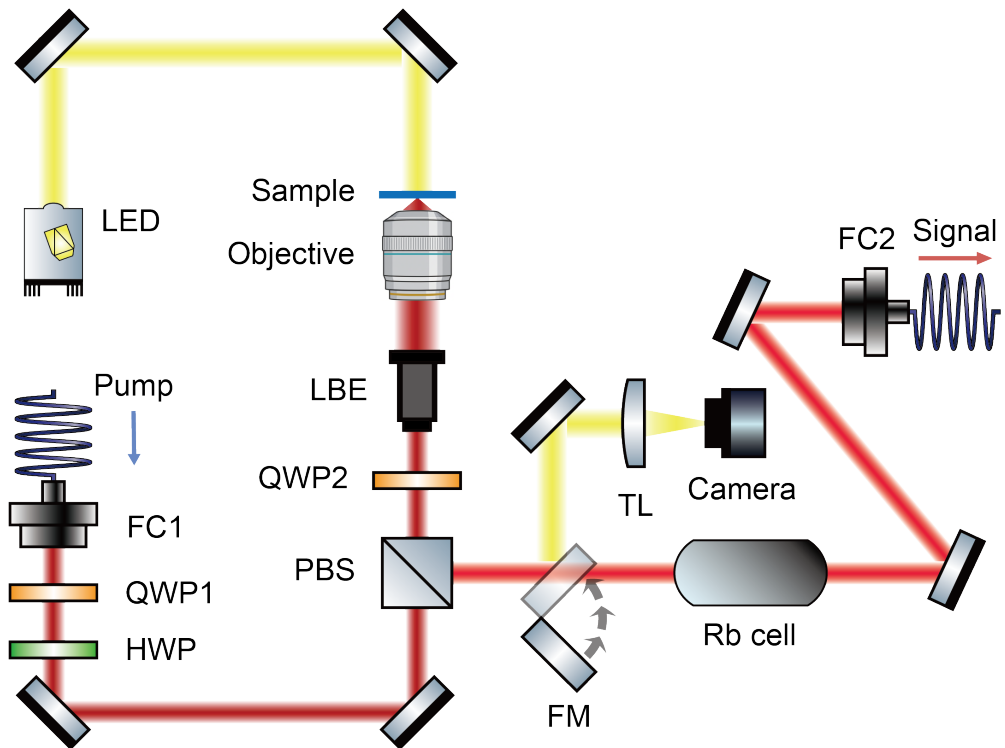
**Supplementary Fig. 1 Characterization of the thermal noise and shot noise of local oscillator.** Noise spectral density of the detection system, including the balanced photodetector and digitizer, as a function of frequency for different local oscillator powers. The trace labeled 0 mW corresponds to the thermal noise floor of the detection system. As the local oscillator power increases, the measured noise rises linearly due to the contribution of optical shot noise, which becomes dominant when the local oscillator power is above 8 mW. In our experiments, we selected a 9 mW local oscillator power to ensure shot-noise limited detection while keeping the power below the saturation level of the balanced photodetector.



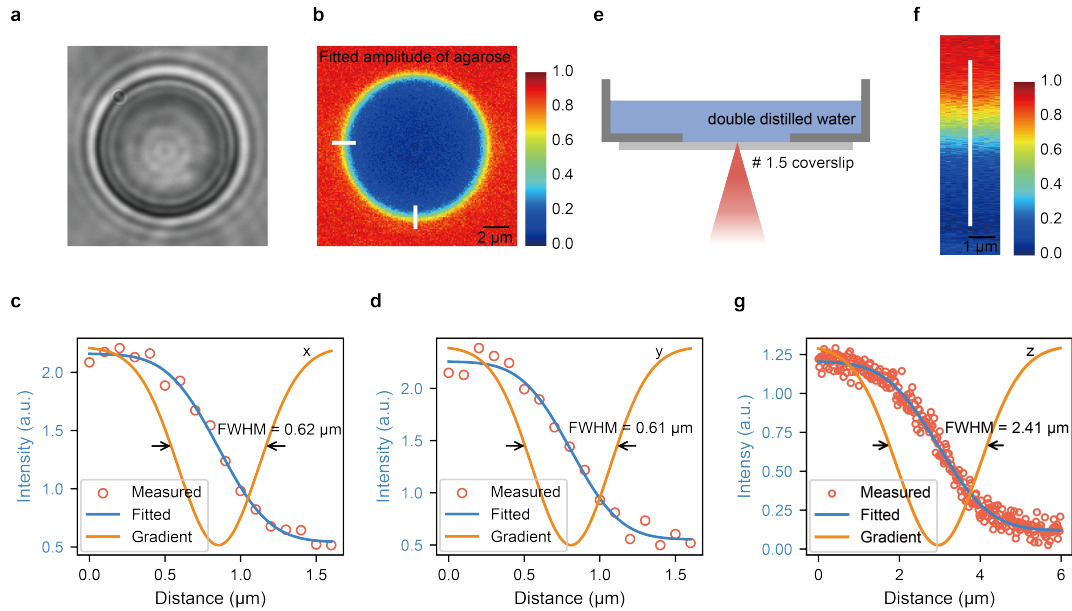
**Supplementary Fig. 2 Characterization of spectral resolution.** **a**, Measured full width at half maximum (FWHM) of the laser spectrum with a fixed pulse width of 204.8 ns as a function of fast Fourier transform (FFT) window duration. When the FFT window duration decreases below 20 ns, the measured FWHM of the laser increases sharply. **b**, Measured FWHM of the laser spectrum with a fixed FFT window duration of 25.6 ns as a function of pulse width. An offset arising from the 25.6-ns FFT window duration is subtracted from the data prior to inverse-proportional fitting. With a fixed FFT window, only a slight increase ( $\sim 5$  MHz) in FWHM is observed when the pulse width decreases from 204.8 ns to 25.6 ns. The pulse widths used for imaging are highlighted by the green shaded region. **c**, Typical laser spectrum measured with the heterodyne detection system. Both the pulse width and FFT window duration are set to 25.6 ns. Appropriate zero-padding is applied to improve the accuracy of Gaussian fitting. **d**, Measured Brillouin linewidths of double-distilled water with different pulse widths and corresponding FFT window durations with a low NA (0.12) objective. Error bars indicate the standard deviation of linewidths extracted from  $n = 400$  individual spectra. An offset of 263.7 MHz, corresponding to the intrinsic linewidth of double-distilled water, is subtracted from the measured linewidth prior to inverse-proportional fitting.



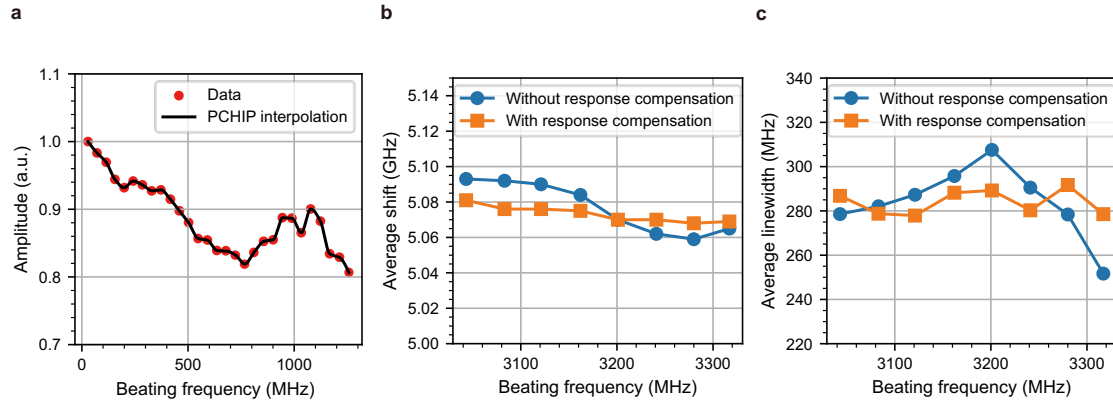
**Supplementary Fig. 3 Dependence of spectral variance on pump peak power.** The spectral variance of the measured water spectra is plotted as a function of frequency for different pump peak powers. Each variance curve is calculated from 400 individual raw spectra acquired under the same pulse width (36 ns), repetition rate (10 kHz), and exposure time (10 ms). To eliminate the influence of nonuniform background noise on visualization—primarily originating from the shot noise of the local oscillator and modulated by the detector response—the baseline variance floor was subtracted. The results clearly show that signal-induced noise dominates when the peak power reaches 28 W, while the average power remains fixed at 10 mW.



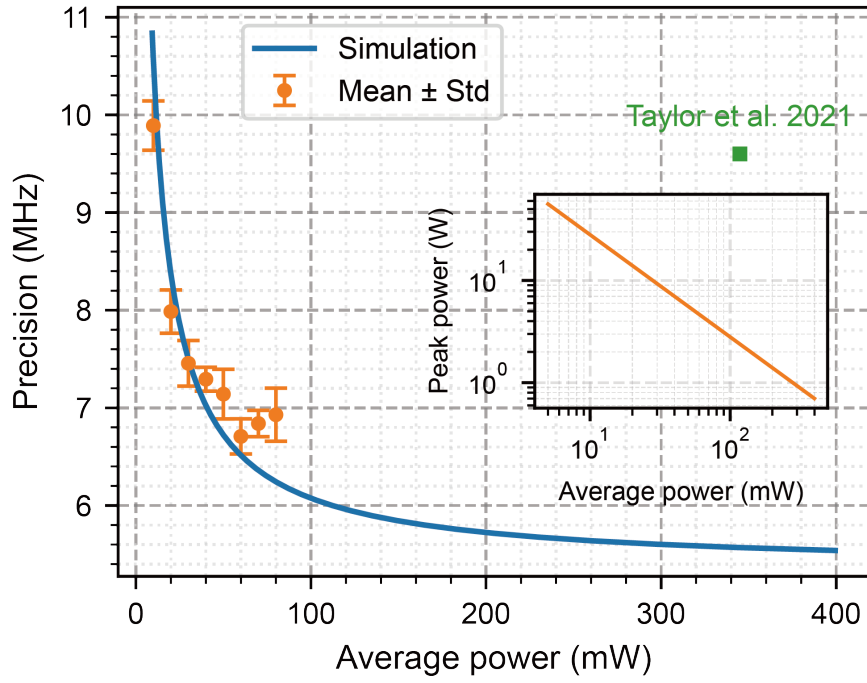
**Supplementary Fig. 4 Detailed setup of PHBM.** LED: light emitting diode; FC: fibre collimator; QWP: quarter-wave plate; HWP: half-wave plate; LBE: laser beam expander; PBS: polarizing beam splitter; FM: flip mirror; TL: tube lens; Rb cell: rubidium cell. The quarter-wave plate and half-wave plate ensure the incident pump transmitting the PBS with minimal power loss. The optical paths for bright-field and Brillouin imaging modes are switched by the flip mirror. With the flip mirror up, the yellow beam carrying the bright-field information is imaged onto the camera. When the flip mirror is down, the Brillouin signal (red beam) passes through the Rb cell and is coupled into the signal fibre.



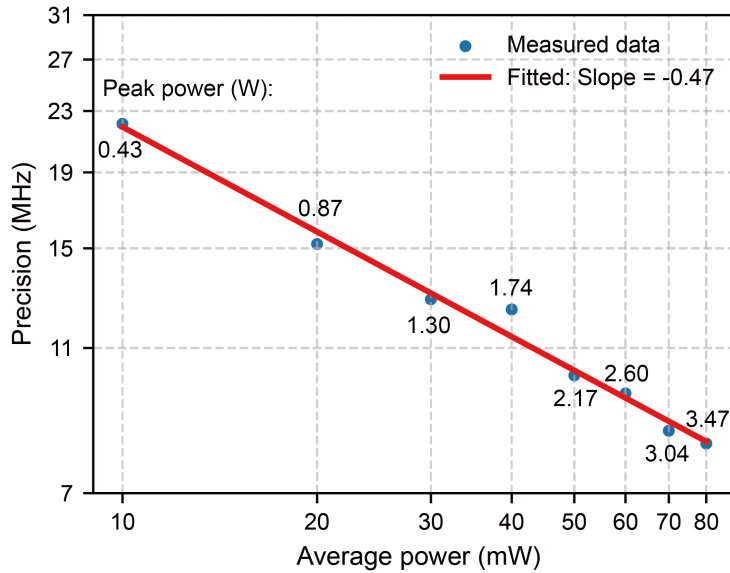
**Supplementary Fig. 5 Spatial resolution characterization of the PHBM.** **a**, Brightfield image of a polymethyl methacrylate (PMMA) bead embedded in agarose. **b**, Normalized Lorentzian fitting amplitude of Brillouin singal from agarose. Since the Brillouin shift of PMMA lies outside the detected spectral range, a single Lorentzian fitting is applied to all measured spectra. **c,d**, Amplitudes of the Lorentzian fits along the x (**c**) and y (**d**) direction across the boundary of the PMMA bead, as indicated by the white solid lines in **b**. The blue and orange lines represent the error function fitting and their corresponding gradients, respectively. **e**, Schematic diagram of the water-glass interface. **f**, Normalized Lorentzian fitting amplitude of Brillouin signal from double distilled water. The Brillouin shift of the coverslip also lies outside the detection range, ensuring that it does not affect the single Lorentzian fitting. **g**, Amplitude profile along the z direction across the boundary between water and the coverslip, as indicated by the white solid line in **f**. The blue and orange lines in represent error function fitting corresponding gradient, respectively.



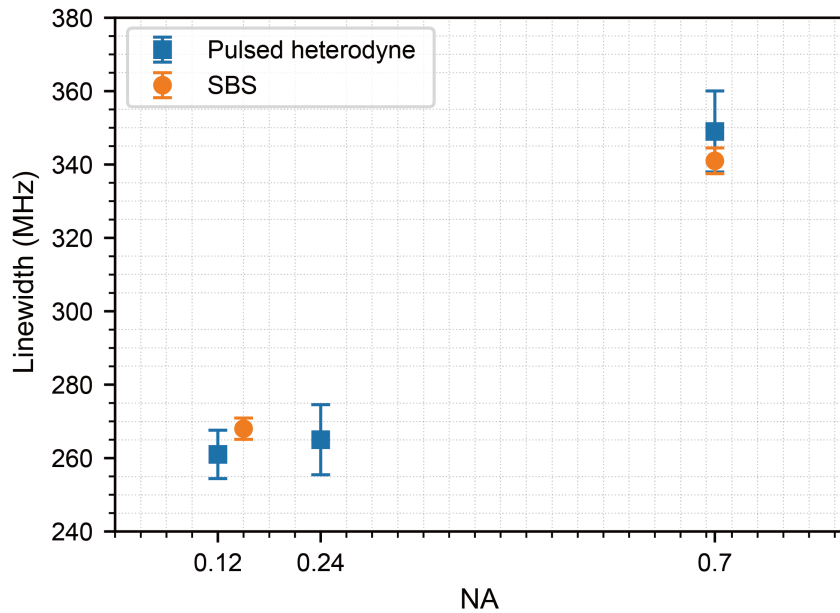
**Supplementary Fig. 6 Balanced photodetector (BPD) frequency response and the spectrum compensation.** **a**, BPD response coefficient at different beating frequencies. The beating signal is generated by two lasers, each with a power of 0.2 mW and detected using an electronic spectrum analyzer. The piecewise cubic Hermite interpolating polynomial (PCHIP) interpolation provides more accurate compensation when the FFT frequency points fall between the interval of measured data. **b**, Comparison of the Brillouin shift of water for different pump–LO frequency differences (before frequency doubling) with (squares) and without (circles) response compensation. **c**, Comparison of the Brillouin linewidth of water for different pump–LO frequency differences (before frequency doubling) with (squares) and without (circles) response compensation. The water signals are measured under an average power of 35 mW and an exposure time of 20 ms. After compensating for the BPD response, the variations in both Brillouin shift and linewidth across different pump–LO frequency differences are reduced, indicating improved spectral measurement accuracy. The BPD’s frequency response is stable and needs to be characterized only once, after which no further maintenance is required.



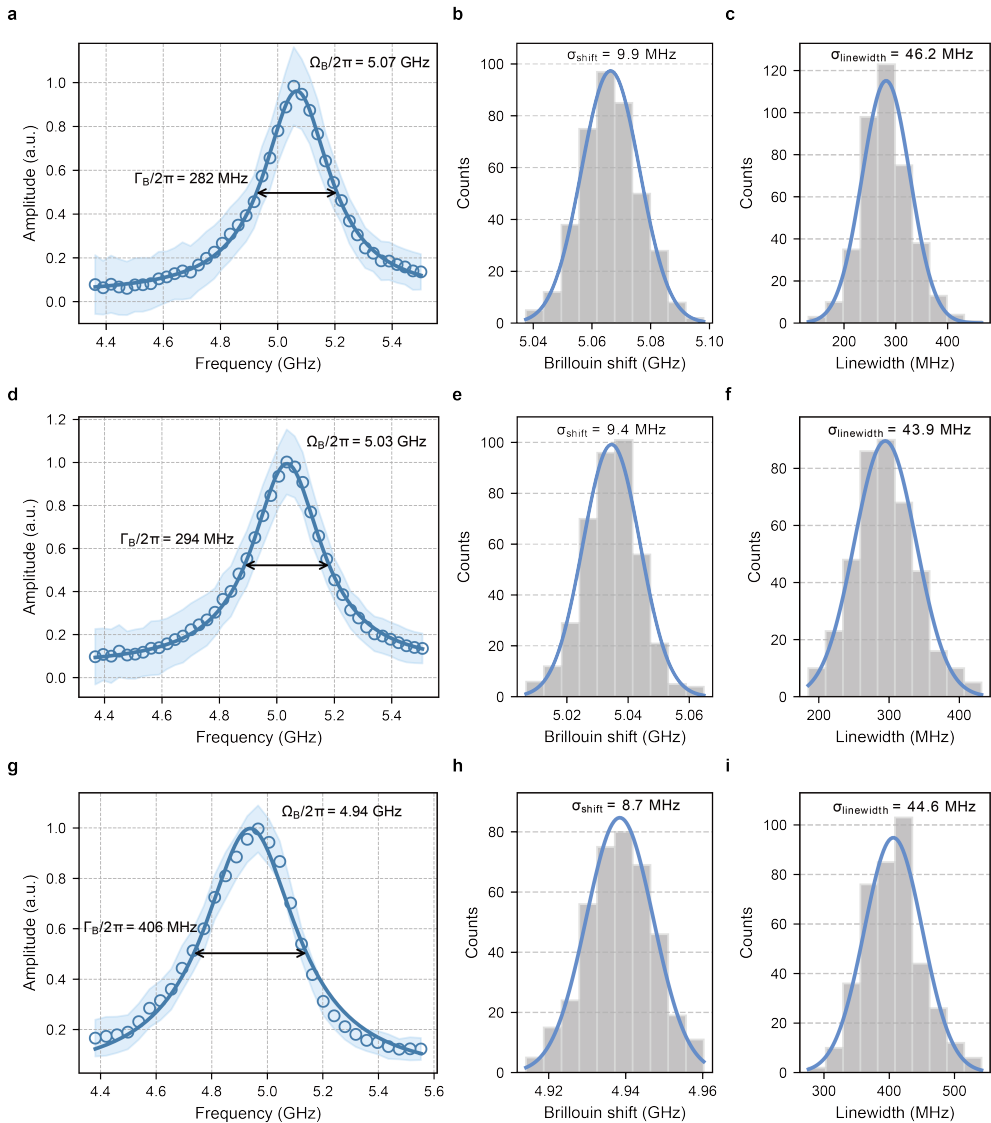
**Supplementary Fig. 7 Theoretical and experimental investigation of measured precision of water as a function of average power.** The main panel plots the measured precision of the Brillouin shift of water as a function of the average optical power. The solid blue line represents the theoretical simulation, while the orange circles with error bars indicate the experimental data (mean  $\pm$  standard deviation). The standard deviation is derived from five independent measurements, with the precision of each measurement estimated from  $n = 400$  Brillouin spectra. For comparison, a result from Supplementary Fig. S3b in Ref. [1] is shown as a green square. All precisions are evaluated under the same exposure time of 10 ms per spectrum. The inset shows the corresponding peak powers used in the simulation for different average powers. Our PHBM markedly enhances energy efficiency, achieving a 35-fold reduction in average power for water measurements at the same exposure time, and an overall 100-fold energy reduction (10-fold in average power and 10-fold in pixel dwell time) for biological imaging, compared with previous work [1].



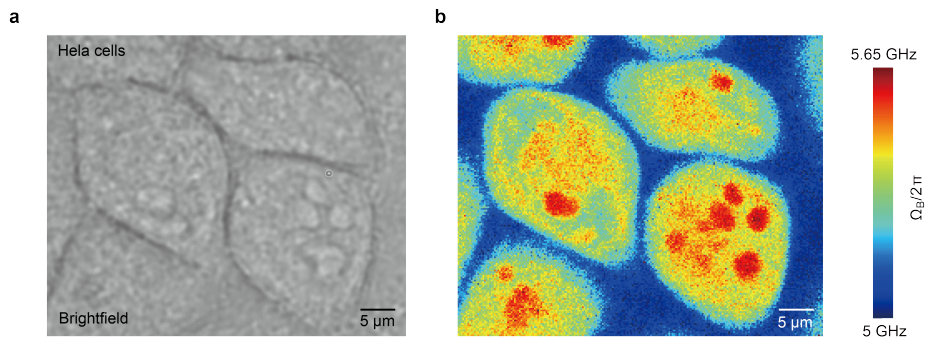
**Supplementary Fig. 8 Characterization of VIPA-based Brillouin spectrometer for comparison.** The measured Brillouin shift precision of water is plotted as a function of average powers of the pump laser. The exposure time per spectrum, pulse width and repetition rate is fixed at 10 ms, 36 ns and 640 kHz, respectively. The increase in average power was achieved by proportionally increasing the peak power, as indicated in the figure. The fitted slope of  $-0.47$  indicates that the VIPA-based spectrometer operated in a shot-noise-limited regime, where the excitation energy is the dominant factor.



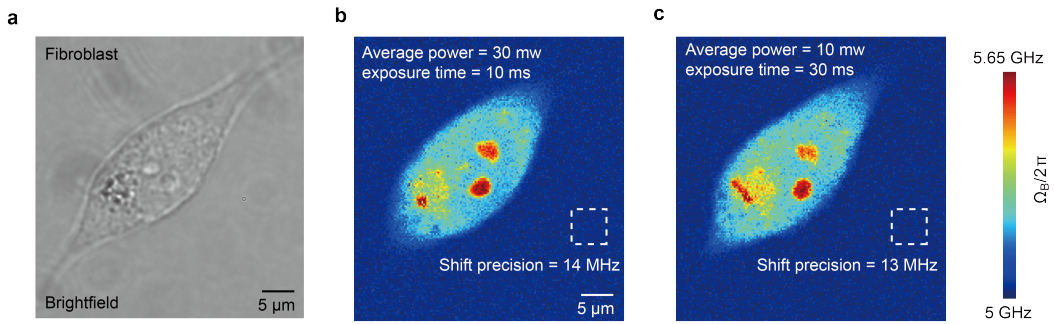
**Supplementary Fig. 9 Comparison of the Brillouin linewidth of water at different NAs in PHBM and stimulated Brillouin scattering (SBS) microscopy.** Brillouin linewidths of double-distilled water measured using PHBM and quasi-pulsed SBS microscopy under different NAs. For the SBS measurements, the exposure times were set to 150 ms (for 0.15 NA) and 100 ms (for 0.7 NA), while the noise-equivalent power bandwidth of the lock-in amplifier was fixed at 800 Hz for a pulse width of 60 ns to minimize additional broadening from the detection system. The average powers on sample for the probe and pump beams were set to 35 mW and 48 mW (for 0.15 NA) and 24 mW and 34 mW (for 0.7 NA), respectively, with an identical duty cycle of 5.2% to ensure a high SNR for accurate measurements. For the PHBM measurements, the pulse width was set to 36 ns, introducing an effective FFT window that resulted in an overall spectral broadening of 27 MHz, including ~4 MHz from the finite pulse duration. The average power, peak power and exposure time were set to 45 mW, 22 W and 200 ms (for 0.12 NA); 10 mW, 21 W and 200 ms (for 0.24 NA); and 30 mW, 28 W and 200 ms (for 0.7 NA), respectively, achieving linewidth precisions of 6.6, 9.6 and 11.0 MHz. All aforementioned spectral broadening contributions were subtracted to obtain the linewidths solely associated with NA-induced broadening shown in the figure. Error bars represent the standard deviation of linewidths extracted from  $n = 400$  individual spectra. The linewidths measured by the two methods agree well, confirming the accuracy of the spectra obtained with PHBM.



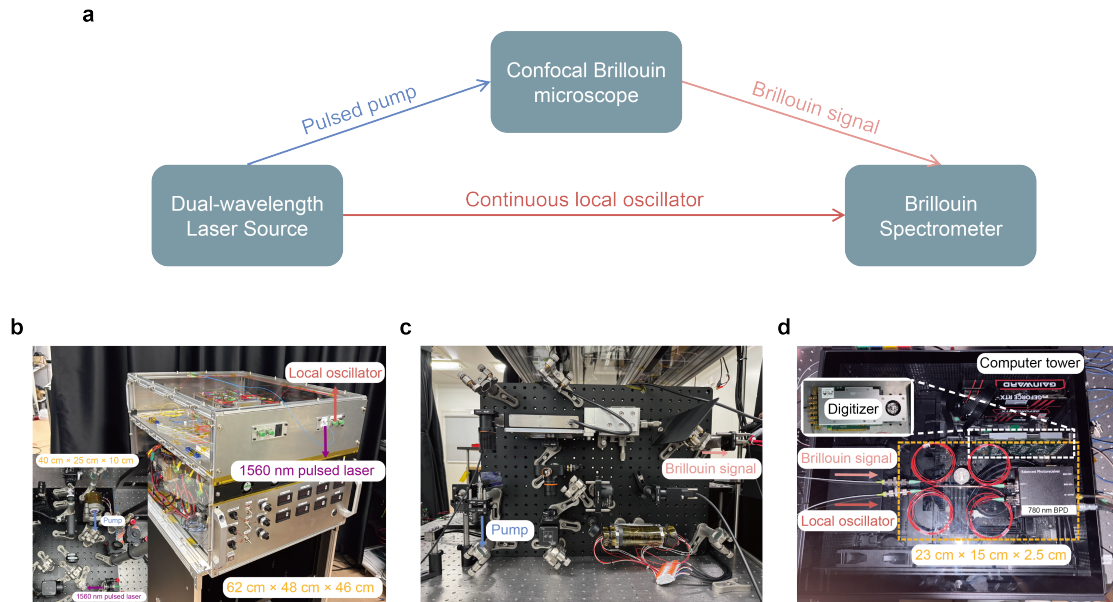
**Supplementary Fig. 10 Performance characterization of PHBM with low-NA (0.12), medium-NA (0.24) and high-NA (0.7) objectives.** **a**, Brillouin spectra of water measured with an average power of 10 mW, exposure time of 10 ms, peak power of 28 W and pulse width of 36 ns using a NA of 0.12. The open circles denote the mean of  $n = 400$  spectra, light blue shading indicates the standard deviation, and solid blue lines are the corresponding Lorentzian fit. **b,c**, Histograms of the Lorentzian-fitted Brillouin shift (**b**) and linewidth (**c**) from spectral in **a**, with the blue curves representing Gaussian fitting. **d**, Brillouin spectra of water measured using a 0.24 NA objective under the same average power, exposure time and pulse width as in **a**, but with a peak power of 21 W. **e,f**, Histograms of the Lorentzian-fitted Brillouin shift (**e**) and linewidth (**f**) from spectral in **d**, with the blue curves representing Gaussian fitting. **g**, Brillouin spectra of water measured using a 0.7 NA objective with an average power of 30 mW, an exposure time of 10 ms, peak power of 33 W, and pulse width of 25.6 ns. **h,i**, Histograms of the Lorentzian-fitted Brillouin shift (**h**) and linewidth (**i**) from spectral in **g**, with the blue curves representing Gaussian fitting.



**Supplementary Fig. 11 PHBM imaging of additional cell line. a**, The brightfield of the imaged HeLa cells. **b**, Brillouin shift of the imaged HeLa cell cluster. Pixel time and average power on sample are respectively 10 ms and 30 mW, with pixels of  $220 \times 181$  and pixel step of  $0.25 \mu\text{m}$ .



**Supplementary Fig. 12 Fibroblast cell images employing different energy distribution strategies.** **a**, Bright-field image of a fibroblast cell. **b,c**, Brillouin shift maps of the cell acquired using a high-power, short-exposure strategy (30 mW, 10 ms) and a low-power, long-exposure strategy (10 mW, 30 ms). Brillouin shift precision of the cell medium region indicated by the dashed box, are highly comparable. Note that the average power was adjusted by varying the pump laser's repetition rate while the peak power was held constant.



**Supplementary Fig. 13 Modular architecture of PHBM.** **a**, Schematic of the three main modules of the PHBM and their interconnections. **b–d**, Photographs of the dual-wavelength laser source (**b**), the microscope optical setup (**c**), and the heterodyne-based Brillouin spectrometer with the processing computer (**d**). The laser system (**b**) consists of a laser-source mainframe and a pulsed-laser second-harmonic generation (SHG) unit. The mainframe measures  $62 \times 48 \times 46 \text{ cm}^3$  and contains three internal layers. The bottom layer houses two seed-laser modules, three single-mode-fibre coupled pump diodes, one multi-mode-fibre coupled pump diode, their corresponding diode drivers, thermoelectric cooler (TEC) controllers, communication and control electronics, voltage converters, and air-cooling components. The second layer contains the fibre-amplifier chains for the short-wave infrared (SWIR) pulsed pump and LO seed. The top layer is dedicated to SHG of the local oscillator (LO) beam. The mainframe outputs the 1560 nm pulsed laser and the 780 nm CW LO beam through respectively a PM1550-XP fibre pigtail and a PM780-HP fibre coupled FC/APC flange connector on the upper front panel. The upper back panel includes three PM1550-XP fibre-coupled FC/APC flange connectors for the seed laser output to the acousto-optic modulator (AOM) chopper, the input of chopped seed pulses, and the seed-beating output. The lower front panel is equipped with switches and knobs for manual control, LED segment displays for real-time status monitoring, and USB interface for communication and advanced control. The mainframe is powered by the 220 V AC mains via a power cord. The PM1550-XP fibre carrying the 1560 nm pulsed laser is connected to the SHG unit (shown in the inset) for frequency doubling, followed by spectral filtering and fibre coupling to the microscope. The main body of the microscope (**c**) is constructed on a breadboard and implements a compact confocal epi-illumination optical layout. It is worth noting that the optical configuration can be readily adapted to a commercial fluorescence microscope in either an upright or inverted geometry. The spectrometer (**d**) consists of only three components: a polarization-maintaining fibre coupler (FC), a balanced photodetector (BPD), and a digitizer. Because the digitizer is directly integrated into the processing computer tower, the effective volume of the heterodyne-based spectrometer is merely  $23 \times 15 \times 2.5 \text{ cm}^3$ , without requiring any additional shielding to block stray light.

**Supplementary Table 1. Summary of results from different spontaneous BM systems**

	Confocal BM (TFP) [1,2]	Confocal BM (VIPA) [3,4]	Line-scanning BM [5,6]			Full-field BM [7]	CW heterodyne [8]	This work (pulsed heterodyne)
Optical configuration	Single – end	Single – end	Orthogonal		Single – end	Orthogonal	Single – end	Single – end
Spectral resolution (MHz) (including NA broadening)	/	550 <sup>a</sup>	/	/	/	> 500 <sup>b</sup>	107 <sup>c</sup>	142 <sup>d</sup>
Intrinsic spectral resolution (MHz) (excluding NA broadening)	100 <sup>e</sup>	500 <sup>f</sup>	250 <sup>g</sup>	510 <sup>g</sup>	510 <sup>g</sup>	/	3.1 <sup>h</sup>	27.4 <sup>i</sup>
Pixel time (ms)	10000 <sup>j</sup>	100	1	1	1	0.024	10 <sup>k</sup> ~100 <sup>l</sup>	10
Average optical power (mW)	17 <sup>j</sup>	3 <sup>m</sup> ~4 <sup>f</sup>	370	18	18	70	276 <sup>l</sup> ~345 <sup>k</sup>	30
Pixel excitation energy ( $\mu$ J)	170000	300 <sup>m</sup> ~400 <sup>f</sup>	370	18	18	1.7	3450 <sup>k</sup> ~27600 <sup>l</sup>	300
Shift precision (MHz)	/	7.5 <sup>m</sup> ~10 <sup>f</sup>	10	19	12.8	83	9.5 <sup>k</sup>	8.7
Linewidth precision (MHz)	/	10 <sup>m</sup>	/	/	/	240	/	45
Spatial resolution, x × y × z ( $\mu$ m <sup>3</sup> )	0.5×0.5 ×8 <sup>e</sup>	x×y: 1.5×1.5 <sup>m</sup> z: /	1.6×1.6 ×4	1.1×0.8 ×1.2	1.1×0.6 ×3.9	x×y: 1.2×1.2 z: /	0.75×0.75 ×4.2	0.62×0.61 ×2.41

TFP: tandem Fabry-Perot; VIPA: virtual image phased array; CW: continuous wave

- [1] Mattana, S. et al. Non-contact mechanical and chemical analysis of single living cells by microspectroscopic techniques. *Light Sci Appl* **7**, 17139 (2018).
- [2] Scarponi, F. et al. High-Performance Versatile Setup for Simultaneous Brillouin-Raman Microspectroscopy. *Phys. Rev. X* **7**, 031015 (2017).
- [3] Scarcelli, G. et al. Noncontact three-dimensional mapping of intracellular hydromechanical properties by Brillouin microscopy. *Nat. Methods* **12**, 1132-1134 (2015).
- [4] Keshmiri, H. et al. Brillouin light scattering anisotropy microscopy for imaging the viscoelastic anisotropy in living cells. *Nat. Photon* **18**, 276–285 (2024).
- [5] Zhang, J. et al. Rapid biomechanical imaging at low irradiation level via dual line-scanning Brillouin microscopy. *Nat. Methods* **20**, 677–681 (2023).
- [6] Bevilacqua, C. et al. High-resolution line-scan Brillouin microscopy for live imaging of mechanical properties during embryo development. *Nat. Methods* **20**, 755–760 (2023).
- [7] Bevilacqua, C. et al. Full-field Brillouin microscopy based on an imaging Fourier-transform spectrometer. *Nat. Photon.* **19**, 494–501 (2025).
- [8] Taylor, M. A. et al. Heterodyne Brillouin microscopy for biomechanical imaging. *Biomed. Opt. Express* **12**, 6259–6268 (2021).

- a. Including NA (0.6) induced spectral broadening extracted from Ref [3].
- b. Estimated from the measured oil linewidth of 1.51 GHz presented in Fig. 2e [7].
- c. Estimated by adding the NA (0.7)-induced spectral broadening (104 MHz for water at 780 nm) to the intrinsic spectral resolution. The 104 MHz broadening is derived by subtracting pulse broadening of 5 MHz, FFT processing broadening of 33 MHz and intrinsic linewidth of 263.7 MHz from measured linewidth in Supplementary Fig. 10g.
- d. Extracted from experiment data by subtracting the intrinsic linewidth of double-distilled water from the measured water spectral linewidth (Supplementary Fig. 10g) using a pulse width of 25.6 ns.
- e. Extracted from Ref [1].
- f. Extracted from Ref [3].
- g. Extracted from direct measurements of a narrow-linewidth laser (typically <1 MHz) spectrum.
- h. Determined from theoretical analysis via time-frequency relationship of the FFT in Ref [8].
- i. Obtained from the fitted curve (Supplementary Fig. 2a, b) at the point of 36 ns pulse width.
- j. Extracted from Ref. [2].
- k. Water measurement extracted from Fig. S3b in Ref. [8].
- l. Biological cell imaging.
- m. Extracted from Fig. 1d in Ref [4].

## Supplementary Note 1. Derivation of SNR for PHBM

We have recently analyzed the general noise model of heterodyne detection in Ref [2]. Here, we simplify the model for our microscopy configuration and provide detailed derivations of the signal expression tailored to our configuration, along with the corresponding noise contributions and the resulting signal-to-noise ratio (SNR), as outlined below.

The electric field of spontaneous Brillouin scattering signal and the local oscillator (LO) can be described as:

$$\tilde{\mathbf{E}}_{Sp}(t) = \hat{x}E_{Sp}(t)e^{i[2\pi f_{Sp}t + \varphi_{Sp}(t)]} \quad (1)$$

$$\tilde{\mathbf{E}}_{LO}(t) = \hat{x}E_{LO}e^{i2\pi f_{LO}t} \quad (2)$$

where  $E_{Sp}$  and  $E_{LO}$  are the field amplitudes,  $f_{Sp}$  and  $f_{LO}$  are the carrier frequencies of the Brillouin signal and the LO, respectively, and  $\varphi_{Sp}$  is the phase difference between them. In our polarization-maintaining configuration, all optical fields are aligned along the same polarization direction  $\hat{x}$ ; therefore, the vector nature of the electric fields can be safely neglected in the following derivation.

After interference in the  $2 \times 2$  fibre coupler with 50:50 splitting ratio, the resulting beat signal at two output ports is written as:

$$\begin{bmatrix} \tilde{E}_{C1}(t) \\ \tilde{E}_{C2}(t) \end{bmatrix} = \begin{bmatrix} \frac{1}{\sqrt{2}} & i\frac{1}{\sqrt{2}} \\ i\frac{1}{\sqrt{2}} & \frac{1}{\sqrt{2}} \end{bmatrix} \begin{bmatrix} \tilde{E}_{Sp}(t) \\ \tilde{E}_{LO}(t) \end{bmatrix} \quad (3)$$

The optical powers reaching the two ports of the balanced photodetector (BPD) can then be calculated as:

$$\begin{aligned} P_{C1}(t) &= \frac{A_{eff}\epsilon_0 c}{2} |\tilde{E}_{C1}(t)|^2 \\ &= \frac{A_{eff}\epsilon_0 c}{4} E_{Sp}^2(t) + \frac{A_{eff}\epsilon_0 c}{4} E_{LO}^2 + \frac{A_{eff}\epsilon_0 c}{2} E_{Sp}(t)E_{LO}\sin[2\pi f_d t + \varphi_{Sp}(t)] \end{aligned} \quad (4)$$

$$\begin{aligned} P_{C2}(t) &= \frac{A_{eff}\epsilon_0 c}{2} |\tilde{E}_{C2}(t)|^2 \\ &= \frac{A_{eff}\epsilon_0 c}{4} E_{Sp}^2(t) + \frac{A_{eff}\epsilon_0 c}{4} E_{LO}^2 - \frac{A_{eff}\epsilon_0 c}{2} E_{Sp}(t)E_{LO}\sin[2\pi f_d t + \varphi_{Sp}(t)] \end{aligned} \quad (5)$$

where  $A_{eff}$  is the effective optical signal area on PD,  $\epsilon_0$  is the vacuum permittivity,  $c$  is the vacuum light speed,  $f_d = f_{Sp} - f_{LO}$  is the frequency difference between Brillouin signal and LO, i.e., the beating frequency. The differential output signal of BPD is then expressed as:

$$\begin{aligned} s(t) &= \mathcal{R}_p A_{eff} \epsilon_0 c E_{Sp}(t) E_{LO} \sin[2\pi f_d t + \varphi_{Sp}(t)] \\ &= 2\mathcal{R}_p \sqrt{P_{Sp}(t)P_{LO}} \sin(2\pi f_d t + \varphi_{Sp}(t)) \end{aligned} \quad (6)$$

where  $\mathcal{R}_p$  denotes the responsivity of the detector, and  $P_{Sp}$  and  $P_{LO}$  are the optical powers of the Brillouin signal and LO, respectively.

In the heterodyne detection scheme, the measured signal is accompanied by a white noise component  $e(t)$ , which mainly consists of thermal noise and shot noise. The power spectral

density (PSD) of the total detection noise is:

$$\sigma_e^2 \approx \sigma_T^2 + 2q\mathcal{R}_p P_{LO} \quad (7)$$

where  $\sigma_T^2$  is the thermal noise contribution and  $q$  is the elementary charge. Since the LO power is typically in the milliwatt range and the spontaneous Brillouin signal is on the picowatt level, the shot noise from the signal itself can be neglected compared to that of the LO.

After digitization with a sampling rate of  $f_s$ , the response of the BPD, including both signal and noise, can be expressed as:

$$r(n) = s(n) + e(n), \quad n = 1, 2, 3, \dots, N_s, \quad (8)$$

where  $N_s$  is the total number of sampled points. To obtain the spectrum, a discrete fast Fourier transform (FFT) is applied to  $r(n)$ , yielding:

$$R(k) = S(k) + E(k), \quad k = 1, 2, 3, \dots, N_s, \quad (9)$$

Since the spontaneous Brillouin spectrum represents a power spectrum, the PSD of the frequency-domain response is of primary interest. Therefore, the norm square of both sides of Eq. (9) is taken to obtain the PSD of  $R(k)$  and normalized by the sampling point number  $N_s$  as follows:

$$\frac{|R(k)|^2}{N_s} = \frac{|S(k)|^2}{N_s} + \frac{|E(k)|^2}{N_s} + \frac{2S_{Re}(k)E_{Re}(k) + 2S_{Im}(k)E_{Im}(k)}{N_s} \quad (10)$$

For determining the overall SNR characterization, three terms in the right side of Eq. (10) are respectively analyzed for clarity.

The measured signal is determined solely by the mean value of the first term on the right side of Eq. (10). By invoking Parseval's theorem directly, rather than employing an auxiliary function like in Ref. [2], the correspondence between the power of the time-domain signal and its frequency-domain representation can be expressed as follows:

$$\sum_{k=1}^{N_s} \frac{|S(k)|^2}{N_s} = \sum_{n=1}^{N_s} \overline{|s(n)|^2} = 2N_s \mathcal{R}_p^2 P_{LO} \bar{P}_{Sp}(t) \quad (11)$$

Considering the single-side PSD case and noting that the spectrum measured in Brillouin microscopy typically follows a Lorentzian line shape, the summation on the left-hand side can be further expressed as

$$\sum_{k=1}^{\frac{N_s}{2}} \frac{|S(k)|^2}{N_s} = \sum_{k=1}^{\frac{N_s}{2}} \frac{|S(k_d)|^2}{N_s} \frac{\gamma_B^2}{\gamma_B^2 + 4(k - k_d)^2} \quad (12)$$

where  $\gamma_B$  denotes the linewidth of the Lorentzian line shape and  $k_d$  represents the spectral index corresponding to the carrier frequency  $f_d$  on a single side of the spectrum. This index can be calculated as:

$$k_d = \frac{f_d}{f_s/N_s} + 1 \quad (13)$$

In heterodyne detection, the sampling bandwidth is chosen to be much larger than the Brillouin linewidth to recover the full Brillouin spectrum. For a sufficiently large number of sampling points  $N_s$ , the summation in Eq. (12) after multiplying the spectral step approaches:

$$\lim_{\delta \rightarrow 0} \delta \sum_{k=1}^{\frac{N_s}{2}} \frac{|S(k_d)|^2}{N_s} \frac{\gamma_B^2}{\gamma_B^2 + 4(k - k_d)^2} = \frac{\pi}{2} \frac{|S(k_d)|^2}{N_s} \gamma_B \quad (14)$$

where  $\delta = \frac{f_s}{N_s}$  denotes the spectral step. Consequently, one can relate Eq. (11), (12) and (14) as follows:

$$\frac{|S(k_d)|^2}{N_s} = \frac{2f_s}{\pi\gamma_B} \mathcal{R}_p^2 P_{LO} P_{Sp}(t) \quad (15)$$

Thus, the expected value of  $\frac{|S(k_d)|^2}{N_s}$  can be directly expressed as:

$$\overline{\frac{|S(k_d)|^2}{N_s}} = \frac{2f_s}{\pi\gamma_B} \mathcal{R}_p^2 P_{LO} \bar{P}_{Sp} \quad (16)$$

Considering the extremely low power of Brillouin signal in microscopy, the variance of  $\frac{|S(k)|^2}{N_s}$  is safely neglected. Consequently, the two main sources of noise arise from the detection noise (originates from second term in Eq. (10)) and the variance of the coupling term (third term in Eq. (10)). Since  $E(k)$  represents the discrete Fourier spectrum of Gaussian white noise, the normalized expected value of  $\bar{E}(k_d)$  at  $k_d$  can be readily calculated as:

$$\overline{\frac{|E(k_d)|^2}{N_s}} = \sigma_e^2 \frac{f_s}{2} \quad (17)$$

In the PHBM system, the bandwidth of the balanced photodetector (BPD) exceeds the sampling bandwidth of the digitizer. Therefore, the effective noise bandwidth is determined by the sampling bandwidth  $\frac{f_s}{2}$ , which is accounted for in Eq. (17). According to the Ref. [3], the variance of Gaussian white noise can be calculated as:

$$D \left\{ \frac{|E(k_d)|^2}{N_s} \right\} \approx \left( \overline{\frac{|E(k_d)|^2}{N_s}} \right)^2 = \frac{1}{4} \sigma_e^4 f_s^2 \quad (18)$$

Another source of noise arises from the coupling term. The variance of the coupling term at  $k = k_d$  can be developed as follows:

$$\begin{aligned}
& D \left\{ \frac{2S_{Re}(k_d)E_{Re}(k_d) + 2S_{Im}(k_d)E_{Im}(k_d)}{N_s} \right\} = \\
& \frac{4}{N_s^2} \overline{[S_{Re}(k_d)E_{Re}(k_d) + S_{Im}(k_d)E_{Im}(k_d)]^2} + \left[ \frac{\overline{2S_{Re}(k_d)E_{Re}(k_d)} + \overline{2S_{Im}(k_d)E_{Im}(k_d)}}{N_s} \right]^2 \\
& = \frac{4}{N_s^2} \left[ \overline{S_{Re}^2(k_d)} \overline{E_{Re}^2(k_d)} + \overline{S_{Im}^2(k_d)} \overline{E_{Im}^2(k_d)} + \overline{2S_{Re}(k_d)E_{Re}(k_d)S_{Im}(k_d)E_{Im}(k_d)} \right] \\
& = \frac{4}{N_s^2} \left[ \overline{S_{Re}^2(k_d)} \overline{E_{Re}^2(k_d)} + \overline{S_{Im}^2(k_d)} \overline{E_{Im}^2(k_d)} \right] \\
& = 2 \frac{\overline{|S(k_c)|^2}}{N_s} \frac{\overline{|E(k_c)|^2}}{N_s} = \frac{2f_s^2}{\pi\gamma_B} \mathcal{R}_p^2 P_{LO} \bar{P}_{Sp} \sigma_e^2
\end{aligned} \tag{19}$$

Here, we have used the following relations:

$$\overline{2S_{Re}(k_d)E_{Re}(k_d)} = \overline{2S_{Im}(k_d)E_{Im}(k_d)} = 0 \tag{20}$$

$$\overline{2S_{Re}(k_d)E_{Re}(k_d)S_{Im}(k_d)E_{Im}(k_d)} = 0 \tag{21}$$

$$\overline{S_{Re}^2(k_d)} = \overline{S_{Im}^2(k_d)} \tag{22}$$

$$\overline{E_{Re}^2(k_d)} = \overline{E_{Im}^2(k_d)} \tag{23}$$

These relations hold when the phases of  $S(k)$  and  $E(k)$  are random, as is the case for both spontaneous Brillouin signals and Gaussian white noise.

Consequently, combining all above analysis, the SNR of the Brillouin spectral peak in a heterodyne-based spontaneous Brillouin spectrometer for biological microscopy can be expressed as:

$$\begin{aligned}
SNR_p &= \frac{\frac{|S(k_d)|^2}{N_s}}{\sqrt{D \left\{ \frac{2S_{Re}(k_d)E_{Re}(k_d) + 2S_{Im}(k_d)E_{Im}(k_d)}{N_s} \right\} + D \left\{ \frac{|E(k_d)|^2}{N_s} \right\}}} \\
&= \frac{\frac{2f_s^2}{\pi\gamma_B} \mathcal{R}_p^2 P_{LO} \bar{P}_{Sp}}{\sqrt{\frac{2f_s^2}{\pi\gamma_B} \mathcal{R}_p^2 P_{LO} \bar{P}_{Sp} \sigma_e^2 + \frac{\sigma_e^4 f_s^2}{4}}} \\
&= \frac{\mathcal{R}_p^2 P_{LO} \bar{P}_{Sp}}{\sqrt{\frac{\pi\gamma_B}{2} \mathcal{R}_p^2 P_{LO} \bar{P}_{Sp} \sigma_e^2 + \frac{\pi^2 \gamma_B^2 \sigma_e^4}{16}}}
\end{aligned} \tag{24}$$

Our SNR expression derived above takes the similar mathematical form as that in Ref. [2], but is explicitly formulated for our PHBM implementation, where the intensity noise of spontaneous Brillouin scattering is negligible owing to its picowatt-level power in biological microscopy.

## Supplementary Note 2. Theoretical analysis of PHBM shift precision

Simulation of the shift precision is performed to evaluate the performance limit of the PHBM system, where the SNR plays a critical role in determining the precision. Therefore, the SNR needs to be further analyzed to correspond to our measurement conditions. For a CW pump laser with total acquisition time  $T$ , the time trace is divided into  $N$  fixed-length temporal intervals of duration  $T_s$ , and the peak SNR of the average spectra obtained from these segments is expressed as:

$$SNR'_p = \sqrt{N}SNR_p = \frac{\sqrt{N}\mathcal{R}_p^2 P_{LO} \bar{P}_{Sp}}{\sqrt{\frac{\pi\gamma_B}{2} \mathcal{R}_p^2 P_{LO} \bar{P}_{Sp} \sigma_e^2 + \frac{\pi^2 \gamma_B^2 \sigma_e^4}{16}}} \\ = \frac{\sqrt{\frac{T}{T_s}} \mathcal{R}_p^2 P_{LO} \bar{P}_{Sp}}{\sqrt{\frac{\pi\gamma_B}{2} \mathcal{R}_p^2 P_{LO} \bar{P}_{Sp} \sigma_e^2 + \frac{\pi^2 \gamma_B^2 \sigma_e^4}{16}}} \propto \frac{\sqrt{T} \mathcal{R}_p^2 P_{LO} \bar{P}_{Sp}}{\sqrt{\frac{\pi\gamma_B}{2} \mathcal{R}_p^2 P_{LO} \bar{P}_{Sp} \sigma_e^2 + \frac{\pi^2 \gamma_B^2 \sigma_e^4}{16}}} \quad (25)$$

On the other hand, the shift precision is inversely proportional to the peak SNR of the detected spectrum and can be expressed as [4]:

$$\sigma_{shift} = \frac{1}{SNR'_p} \sqrt{\frac{3}{4} \times \delta \times \gamma_B} \quad (26)$$

where  $\delta$  and  $\gamma_B$  denote the frequency step and the Brillouin linewidth of the target sample, respectively. The total number of spectral points in each segment  $N_s$  follows the relation  $N_s = f_s \times T_s$ , where  $f_s$  denotes the sampling rate of digitizer, which is set to 2.5 GS/s in the PHBM configuration. Thus, the frequency step can be calculated by

$$\delta = \frac{f_s}{N_s} = \frac{1}{T_s} \quad (27)$$

Note that the shift precision is related with both the SNR and frequency step, resulting in its independence of the segment length  $T_s$ . Considering the confinement of biological imaging, feasibility of laser system and performance of spectral resolution, the CW pump laser is assembled into periodically arranged pulses with a selected  $T_s$  with 20-40 ns duration. Therefore, in the case of a pulsed pump laser, the number of segments averaged to obtain a single spectrum is determined by the pulse repetition rate and total acquisition time. For example, for a 10 ms acquisition time and a 10 kHz repetition rate,  $N = 100$  pulses are integrated and processed according to the data analysis steps described in the Methods. For simulation, the pulse width was fixed at 36 ns, corresponding to a frequency step of 27.8 MHz. Considering spectral broadening introduced by both the finite FFT window and the pulse width, the experimentally measured linewidth of 288 MHz was adopted.

In the simulation, the LO power was set to 9 mW, consistent with the experimental condition where the shot noise dominates (Supplementary Fig. 1), and the total noise can be expressed as:

$$\sigma_e^2 = 2q\mathcal{R}_p P_{LO} \quad (28)$$

The responsivity of the employed BPD is 0.5 A/W. The collected Stokes Brillouin power  $\bar{P}_{Sp}$  under a low effective NA (0.12) objective was estimated to be approximately 7.5 fW for an incident laser power of 1 mW using a VIPA-based spectrometer. This estimation was performed as follows. First, a 1 pW laser beam was directly coupled into the spectrometer obtained by applying a 50 dB optical attenuator to a 100 nW laser. The summed gray value of the laser region on the camera was recorded after subtraction of mean background, while the exposure time was set to 20 ms to ensure a sufficiently high signal such that the pixel-wise background fluctuation could be neglected. After optimizing collection efficiency (see Methods), a CW pump laser with controlled power was focused onto the sample (water in this experiment), and the Brillouin scattering signal was guided into the VIPA for separating the Brillouin signal. The exposure time was set to 200 ms for a sufficiently high signal, as the Brillouin signal is much weaker than the 1 pW laser. After obtaining the Stokes-side gray values (only the stokes Brillouin signal is detected in the PHBM) by subtracting the mean background, the Brillouin scattering power collected under this setup can be calculated by scaling the ratio of total gray value, incident power, and exposure time between the two cases.

Parameters corresponding to the first experimental point were used as a baseline, with a peak power  $P_b = 28 \text{ W}$ , pulse repetition rate  $R_b = 10 \text{ kHz}$ , average power  $A_b = 10 \text{ mW}$ , exposure time  $T_b = 10 \text{ ms}$  and averaging number  $N_b = R_b \times T_b = 100$ . For points with other peak powers  $P_s$  in simulation, parameters were scaled according to the power ratio  $\epsilon = P_s / P_b$ . The repetition rate was scaled as  $R_b / \epsilon^2$  while the average power was set to  $A_b / \epsilon$ . The exposure time was kept constant at  $T_b$ , and the effective averaging number for each simulation point was calculated as  $N_b / \epsilon^2$ .

Simulation and experiment data are exhibited in Supplementary Fig. 7. Since the variation of the coupling term (first term under the square root in the denominator of Eq. (24)) is proportional to the Brillouin signal power, increasing the excitation power correspondingly increases the variance. According to the simulation, the two noise components in Eq. (24) become equal when the peak power reaches 9.7 W, indicating that the pulse enhancement gradually saturates with further increases in peak power, which is consistent with the experimental results (Supplementary Fig. 7). When the peak power rises to 20 W, the total noise becomes dominated by the coupling-term contribution, with the variation ratio reaching approximately 2:1. Once the peak power is sufficiently high such that the Brillouin-signal-dependent noise significantly (first term under the square root in the denominator of Eq. (24)) exceeds the constant noise (second term under the square root in the denominator of Eq. (24)), the SNR becomes proportional to the square root of the Brillouin signal power. Under this condition, increasing the peak power provides the same improvement in SNR as extending the acquisition time, corresponding to a shot-noise-limited performance regime. The minor discrepancy between simulation and experiment may originate from the difference between the estimated and actual responsivity of the BPD, as well as from inaccuracy in the measured Brillouin scattering efficiency of water.

### Supplementary Note 3. Selection of objectives and performance characterization

Representative water measurement results obtained with different objectives are presented in Supplementary Fig. 10. To optimize system performance under various imaging conditions, three types of objectives were employed. The low numerical aperture (NA) objective (ACHN10XP, Olympus) was primarily used to characterize the intrinsic linewidth of water and evaluate the system's performance limit. The incident laser beam diameter (4.4 mm) was smaller than the back aperture of the objective (9 mm), leading to an effective NA of 0.12. Under an average power of 10 mW and an exposure time of 10 ms, the Brillouin shift precision and linewidth precision for water are 9.9 MHz (Supplementary Fig. 10b) and 46.2 MHz (Supplementary Fig. 10c), respectively. A peak power of 28 W was used, resulting in variance of noise from coupling term approximately three times higher than that of the constant noise.

For porcine cornea imaging, an objective with slightly higher NA (ACHN20XP, Olympus) was employed to obtain improved spatial resolution. Since the back aperture of this objective remained larger than the beam diameter, the effective NA was 0.24. With an average power of 10 mW and an exposure time of 10 ms, the Brillouin shift and linewidth precisions reached 9.4 MHz (Supplementary Fig. 10e) and 43.9 MHz (Supplementary Fig. 10f), respectively, when the peak power was 21 W. Notably, a pulse width of 36 ns was used in water measurements for performance characterization, whereas a shorter 25.6 ns pulse was adopted during corneal imaging to achieve a higher peak power. Although the NA increase (0.12) was modest compared with previously mentioned objective, a 12 MHz spectral broadening was observed (Supplementary Fig. 10a, d). The 3-mm working distance of this objective was sufficient for scanning the corneal surface region.

For cell imaging, higher spatial resolution was required to resolve subcellular features. A high-NA objective (LUCPLFLN60X, Olympus) was therefore employed. Due to its relatively low transmittance, a 25.6 ns pulse was used to maintain sufficiently high peak power (32.6 W). Under an average power of 30 mW and an exposure time of 10 ms, the shift precision and linewidth precision reached 8.7 MHz (Supplementary Fig. 10h) and 44.6 MHz (Supplementary Fig. 10i), respectively. The performance degradation observed with this objective is attributed to its lower transmittance compared with the other two objectives. Furthermore, compared with the lower-NA cases, NA-induced spectral broadening was more pronounced, causing the mean Brillouin spectrum of water to deviate from a Lorentzian lineshape (Supplementary Fig. 10g). This spectral distortion may reduce the spectral fitting precision, particularly for linewidth estimation. In addition, a downshift of the Brillouin frequency was observed when using higher NA (Supplementary Fig. 10a, d, g), consistent with the NA-induced spectral broadening predominantly affecting the lower-frequency region [5,6].

#### Supplementary Note 4. Limitations and further developments

Due to the finite sampling rate of the digitizer, the detectable spectral range is limited to 1.25 GHz. For samples exhibiting broader Brillouin spectra, this restriction prevents the acquisition of the complete spectrum, thereby reducing the fitting accuracy of both the Brillouin shift and linewidth. In the proposed PHBM, the local oscillator frequency is set 6 GHz below the pump laser, resulting in two detectable bands: 4.75–6.00 GHz and 6.00–7.25 GHz. Signals with frequencies outside this range (i.e., below 4.75 GHz or above 7.25 GHz) cannot be captured. When the Brillouin spectrum extends across the 6 GHz boundary, spectral components fold and overlap due to frequency aliasing, introducing spectral distortion and inaccuracy in the fitted shift and linewidth.

In PHBM, only the Stokes Brillouin signal is detected. A twofold increase in signal amplitude can be achieved if the anti-Stokes Brillouin signal is also detected. By employing a carrier-suppressed electro-optic modulator (EOM) to generate a double-sideband local oscillator, both Brillouin sidebands can be captured simultaneously. Further improvement in spectral precision, as extended measurement capability for samples with broader linewidths or larger frequency shifts, can be realized by using a BPD with a wider bandwidth and a digitizer with a higher sampling rate.

#### Supplementary References

45. Taylor, M. A. et al. Heterodyne Brillouin microscopy for biomechanical imaging. *Biomed. Opt. Express* **12**, 6259–6268 (2021).
46. Jin, S. et al. A Framework for Spontaneous Brillouin Noise: Unveiling Fundamental Limits in Brillouin Metrology. Preprint at <https://doi.org/10.48550/arXiv.2505.17651> (2025).
47. Oppenheim, A. V. & Schafer, R. W. *Discrete-Time Signal Processing*, 3rd edn (Pearson, Upper Saddle River, NJ, 2010).
48. Soto, M. A. et al. Modeling and evaluating the performance of Brillouin distributed optical fiber sensors. *Opt. Express* **21**, 31347–31366 (2013).
49. Antonacci, G. et al. Spectral broadening in Brillouin imaging. *Appl. Phys. Lett.* **103**, 221105 (2013).
50. Shaashoua, R. et al. Aperture-induced spectral effects in stimulated Brillouin scattering microscopy. *Appl. Phys. Lett.* **122**, 143702 (2023).